Retrieval of H_2O abundance in Titan's stratosphere: a (re)analysis of CIRS/Cassini and PACS/Herschel observations[1]*

S. Bauduin[a], P.G.J. Irwin[a], E. Lellouch[b], V. Cottini[c], R. Moreno[b], C.A. Nixon[d], N.A. Teanby[e], T. Ansty[f], F.M. Flasar[d]

[a] *Atmospheric, Oceanic and Planetary Physics, University of Oxford, Parks Road, Oxford OX1 3PU, UK*
[b] *LESIA-Observatoire de Paris, CNRS, Université Paris 06, Université Paris-Diderot, 5 Place Jules Janssen, 92195 Meudon, France*
[c] *Department of Astronomy, University of Maryland at College Park, College Park, MD 20742, USA*
[d] *Planetary Systems Laboratory, NASA Goddard Space Flight Center, Greenbelt, MD 20771, USA*
[e] *School of Earth Sciences, University of Bristol, Wills Memorial Building, Queens Road, Bristol BS8 1RJ, UK*
[f] *Department of Space Science, Cornell University, Ithaca, NY 14853, USA*

Abstract

Since its first measurement 20 years ago by the Infrared Space Observatory (ISO), the water (H_2O) mole fraction in Titan's stratosphere remains uncertain due to large differences between the determinations from available measurements. More particularly, the recent measurements made from the Herschel observatory (PACS and HIFI) estimated the H_2O mole fraction to be 0.023 ppb at 12.1 mbar. A mixing ratio of 0.14 ppb at 10.7 mbar was, however, retrieved from nadir spatially-resolved observations of Cassini/CIRS. At the same pressure level (10.7 mbar), this makes a difference of a factor of 5.5 between PACS and CIRS measurements, and this has notably prevented current models from fully constraining the oxygen flux flowing into Titan's atmosphere. In this work, we try to understand the differences between

the H_2O mole fractions estimated from Herschel/PACS and Cassini/CIRS observations. The strategy for this is to 1) analyse recent disc-averaged observations of CIRS to investigate if the observation geometry could explain the previous observed differences, and 2) (re)analyse the three types of observation with the same retrieval scheme to assess if previous differences in retrieval codes/methodology could be responsible for the previous discrepancies. With this analysis, we show that using the same retrieval method better reconcile the previous measurements of these instruments. However, the addition of the disc-averaged CIRS observations, instead of confirming the consistency between the different datasets, reveals discrepancies between one of the CIRS disc-averaged set of observations and PACS measurements. This raises new questions regarding the possibility of latitudinal variations of H_2O, which could be triggered by seasonal changes of the meridional circulation. As it has already been shown for nitriles and hydrocarbons, this circulation could potentially impact the latitudinal distribution of H_2O through the subsidence or upwelling of air rich in H_2O. The possible influence of spatial/time variations of the OH/H_2O input flux in Titan's atmosphere is also discussed. The analysis of more observations will be needed in future work to address the questions arising from this work and to improve the understanding of the sources of H_2O in Titan's atmosphere.

Keywords: Titan, atmosphere, Atmosphere, composition, Spectroscopy, Infrared observations, Satellite, atmosphere

[1] *Herschel is an ESA space observatory with science instruments provided by European-led Principal Investigator consortia and with important participation from NASA.*

1. Introduction

Since the discovery of carbon dioxide (CO_2) more than 30 years ago (Samuelson et al., 1983), the presence of oxygen compounds has been firmly demonstrated in Titan's atmosphere. Among these, water vapour (H_2O) is deposited in the high atmosphere by external sources. It was measured for the first time in Titan's stratosphere around 20 years ago by the Infrared Space Observatory (ISO), using the Short Wavelength Spectrometer (SWS) (Coustenis et al., 1998). The two lines recorded at 227.8 and 254 cm^{-1} by this instrument were effectively modelled using a H_2O profile of 0.4 ppb above some cut-off altitude and were mainly sensitive to H_2O in the pressure range 1–1 $\times$ 10^{-5} mbar. After this first detection, de Kok et al. (2007a) made a first attempt to measure stratospheric H_2O with the Composite Infrared Spectrometer (CIRS) on board the NASA Cassini spacecraft. Due to a poor signal-to-noise ratio (SNR), this first analysis of CIRS spectra was unsuccessful, and only an upper limit of 0.9 ppb was determined, which was consistent with ISO observations. These results were, however, later challenged by measurements from the Photodetector Array Camera and Spectrometer (PACS) and the Heterodyne Instrument for the Far-Infrared (HIFI) onboard the Herschel observatory (Moreno et al., 2012). Using both instruments, Moreno et al. (2012) constrained the vertical profile of H_2O, showing that it increases with height, which is consistent with a high altitude source and low-level sink (condensation and photolysis). They retrieved a H_2O volume mixing ratio (VMR) of 0.023 ppb at 12.1 mbar, which is 20-times lower than the VMR (assumed constant with altitude above the saturation level) determined from ISO. Furthermore, Moreno et al. (2012) reanalysed SWS/ISO spectra and

showed that the H_2O abundance inferred from those observations needed a downward revision to 0.06 ppb (uniform profile). Almost at the same time, Cottini et al. (2012) performed a second attempt to measure H_2O from nadir and limb CIRS observations. By averaging a large number of nadir spectra recorded over 4 years, they determined a H_2O VMR of 0.14 ppb at 10.7 mbar. From limb observations, they retrieved 0.13 ppb at 115 km (around 6 mbar) and 0.45 ppb at 230 km (around 0.35 mbar), which confirmed that the H_2O mole fraction increases with height. The retrieved abundance, however, differed by about a factor of 4 from the results of Moreno et al. (2012).

These uncertainties on the H_2O mole fraction have prevented photochemical models from constraining the flux of OH/H_2O into Titan's atmosphere. As a result, it is currently not determined whether the main source of H_2O comes from micrometeorite ablation (English et al., 1996) or from local sources, such as the cryovolcanic activity on Enceladus (e.g. Hansen et al., 2006; Waite et al., 2006; Hansen et al., 2008, 2011). Using HIFI onboard Herschel, Hartogh et al. (2011) detected the Enceladus H_2O torus and proposed that the latter could be the main source of H_2O in Saturn's atmosphere. Based on the OH/H_2O input flux required by the model of Hörst et al. (2008) to reproduce the H_2O abundance retrieved from ISO observations, Hartogh et al. (2011) concluded that the Enceladus influx rates at Titan's atmosphere are too small to explain the observed H_2O abundance. However, with the retrieval of H_2O from Herschel, Moreno et al. (2012) estimated new input fluxes and showed that Enceladus surface activity is a viable source of H_2O in Titan's atmosphere. This was confirmed by the recent model of Dobrijevic et al. (2014), coupling oxygen, nitrogen and hydrocarbon chemistry,

which was able with an Enceladus source to reproduce the H_2O abundance retrieved by either Moreno et al. (2012) or Cottini et al. (2012). Note that if the H_2O abundance retrieved by Cottini et al. (2012) is taken as the reference, Dobrijevic et al. (2014) overestimated the thermospheric H_2O mole fraction when compared with the upper limit estimated by Cui et al. (2009) from the Cassini/INMS (Ion Neutral Mass Spectrometer) data. The OH/H_2O input flux determined is, however, very different depending on the reference chosen. More particularly, if the flux is determined using the results of Moreno et al. (2012), both Moreno et al. (2012) and Dobrijevic et al. (2014) could not reproduce H_2O and CO_2 abundances at the same time. They respectively obtained CO_2 mole fractions 10 and 4 times lower than the observed abundance (de Kok et al., 2007a). Based on the large difference in the atmospheric lifetimes of CO_2 (several hundred years) and H_2O (around 10 years), Moreno et al. (2012) invoked a variable OH/H_2O input flux over long timescales to explain this difference. This scenario has been explored by the recent model of Lara et al. (2014). They showed, however, that when results of Moreno et al. (2012) are considered, a time-dependent input flux does not solve alone the H_2O/CO_2 problem and the addition of another loss term for H_2O, such as a loss to the haze, is required. Understanding the discrepancies between the H_2O mole fractions measured from Herschel and CIRS is therefore crucial to better constrain the existing photochemical models, and to improve the knowledge of the source and chemistry of oxygen compounds in Titan's atmosphere.

In this work, we aim to investigate and understand these previous reported differences. For this, we analyse recent disc-averaged observations

of Titan (2013-2015) made with the CIRS/Cassini instrument and retrieve new H_2O mole fractions. The use of disc-averaged observations allows an easier comparison with Herschel measurements, which share the same viewing geometry. In addition to a difference in observation geometry, Moreno et al. (2012) and Cottini et al. (2012) also applied distinct retrieval methods and used different *a priori* information and radiative transfer modelling codes to retrieve H_2O. The goal of this work is also to (re)analyse the CIRS and Herschel datasets with the same retrieval scheme. This will allow us to distinguish if the observed discrepancies are due to modelling/retrieval differences or due to other possible sources. In the case of Herschel, we focus only on PACS observations, which have a very similar vertical sensitivity to H_2O as the CIRS measurements. Among the spectra analysed by Cottini et al. (2012), we only consider the nadir spectrum for the same reasons. These observations are presented in more details in section 2. Sections 3 and 4 describe, respectively, the forward modelling settings and the retrieval strategy developed to analyse all observations. The results are then discussed in section 5.

2. Instruments and observations

2.1. CIRS

The CIRS instrument is a Fourier transform spectrometer. It is composed of three separate focal planes (FP1, FP3 and FP4) that measure together spectra in the far- and mid-infrared (IR) (full range: 10–1400 cm^{-1}) with an adjustable apodised resolution between 0.5 and 15.5 cm^{-1}. The FP1 covers the far-IR spectral range (10–600 cm^{-1}). It has a circular field-of-view

(FOV) of 3.9 mrad diameter, whose half of the integrated response is located within 2.5 mrad. The FP3 and FP4 focal planes consist of collinear arrays of 10 pixels each that record spectra in the mid-IR range (respectively 600–1100 cm^{-1} and 1100–1400 cm^{-1}). The size of each FOV is 0.27×0.27 mrad. More details about the instrument can be found elsewhere (e.g. Flasar et al., 2004; Jennings et al., 2017).

In this work, four sets of FP1 observations recorded between February 2013 and July 2015 at a spectral resolution of 0.5 cm^{-1} are analysed. They were acquired during four different observations at more than 1.5 million kilometres from Titan (Titan Explorations at Apoapse, TEA), and each set include around 800 disc-averaged spectra. The first observation (rev 182) lasted 20 hours whereas the three next ones (revs 202, 206, 209) lasted around 12 hours. The sub-spacecraft latitudes of these observations are -41.43°, 50.73°, 48.58° and -0.02° respectively for sets 182, 202, 206 and 219. Details of these four sets are given in Table 1.

Because H_2O lines are very weak in the FP1 range, an averaged spectrum has been calculated for each set of observations to increase the SNR. They are shown in Figure 1 for the 125–260 cm^{-1} spectral range. The associated noise has been evaluated using the same method as Teanby et al. (2006). Briefly, two types of standard error are calculated for each set: 1) the standard deviation on the averaged spectrum, and 2) the standard error related to the noise equivalent spectral radiance (NESR) measured from deep space spectra. The maximum of these standard errors is then taken as the measurement error on the averaged spectrum. This measurement error is similar for the four sets, with the minimum found for the 182 (around 1 nW cm^{-2} sr^{-1} cm

for the spectral range shown in Figure 1) and the maximum for the 206 and 219 sets (around 1.4 nW cm^{-2} sr^{-1} cm). Noise spikes are however located in different ranges: 140–150 cm^{-1} for 182, 152–164 cm^{-1} for 202, 212–227 cm^{-1} for 206, and 240–265 cm^{-1} for 219. A spike at 191.25 cm^{-1} is common to all sets.

From Figure 1, we can see that H_2O lines are at most barely detected. This is not surprising given the small number of spectra averaged together. For comparison, Cottini et al. (2012) averaged thousands of nadir spectra to achieve a sufficient SNR. Among the four sets analysed here, the SNR seems to vary, with only set 182 showing clear H_2O lines. For this set, the SNR of the H_2O lines is estimated to be around 2 for the lines located above 200 cm^{-1} and around 3 for the ones below. The difference observed with the other sets is unlikely to be attributable to measurement error differences, the latter being small. The possibility of latitudinal variations will be discussed in section 5.2.4. Note that in section 5.2.1, we will assess if H_2O lines are present in the sets 202, 206 and 219. Note also that the retrieval scheme, which is described in the following sections, has been developed using set 182 only.

Finally, the nadir spectrum studied previously by Cottini et al. (2012) is reanalysed. This spectrum is an average of around 7000 spectra acquired between December 2004 and December 2008 in a latitudinal bin of 0–30°N (see Figure 1). More details are given in Cottini et al. (2012). This averaged spectrum will be called "CIRS NA" hereafter.

2.2. PACS/Herschel

PACS is one of the three science instruments onboard the Herschel observatory. It is composed of an imaging photometer, covering the spectral range 60–210 μm (47.6–181.8 cm^{-1}) over a FOV of $1.75' \times 3.5'$, and of a grating spectrometer, providing observations in the range 55–210 μm at a spectral resolving power between 1000 and 4000 and over a FOV of 47" $\times$47", resolved in 5×5 pixels. More details about the instruments can be found in Poglitsch et al. (2010).

In this work, we reanalyse the spectra recorded by the PACS spectrometer that were previously studied by Moreno et al. (2012). These consist of disc-averaged observations of three H_2O lines at 66.43 μm (150.5 cm^{-1}), 75.38 μm (132.7 cm^{-1}) and 108.07 μm (92.5 cm^{-1}), expressed as line/continuum ratios. They were recorded on 22$^{\rm nd}$ June 2010 when the apparent distance between Titan and Saturn was close to the maximum elongation (see Moreno et al. (2012) for more details about the observations and their reduction). In addition to H_2O lines, observations of CH_4 lines acquired by PACS at around the same time are also analysed to retrieve temperature information. These were recorded in the range 102–146 μm using the chopped-nodded PACS range spectroscopy mode with a small chopper throw (see PACS observers' manual 2013, http : //herschel.esac.esa.int/Docs/PACS/pdf/pacs_om.pdf). In this spectral range, two CH_4 lines have been used in this work, at 106.43 μm (94 cm^{-1}) and 119.63 μm (83.6 cm^{-1}). These CH_4 spectra have been reduced from Level 0 to Level 2 within HIPE 15.0.0 (Herschel Interactive Processing Environment), using the Telescope Normalization pipeline (see PACS Data Reduction Guide 2017 for details, http : //herschel.esac.esa.int/twiki/pub/Pu

blic/PacsCalibrationWeb/pacs_spec15.pdf), and the final spectrum has been rebinned close to the Nyquist sampling. Note that spectra (CH_4 lines only) reduced in such a way have units of Janskys (Jy) and have been converted to spectral radiance units of W cm^{-2} sr^{-1} cm. Table 2 summarizes the PACS observations analysed in this work, which are shown in Figure 1.

3. Forward model

3.1. Reference atmosphere and spectroscopic data

A reference atmosphere has been defined for the analysis of all the observations considered. It is composed of 99 levels distributed between 1457 and 1.01×10^{-5} mbar. The far-infrared spectrum of Titan's atmosphere, and more especially the continuum level, is affected by collision-induced absorption (CIA) between pairs of N_2, CH_4 and H_2 molecules. The CIA coefficients have been calculated using the work of Borysow and Frommhold (1986a,b,c, 1987), Borysow (1991) and Borysow and Tang (1993). The reference vertical profiles of the 3 gases included are shown in Figure 2.a. The profile of CH_4 has been defined according to Niemann et al. (2010) with a volume mixing ratio of around 5.6% close to the surface and of 1.48% in the stratosphere. For H_2, the mixing ratio has been set at 0.101% at all pressure levels (Niemann et al., 2010). In addition to CIA, the continuum shape is also impacted by aerosol absorption. The assumed haze vertical profile is shown in Figure 2.b and is a simplified version built from previous results (de Kok et al., 2007b, 2010b; Tomasko et al., 2008). The haze relative absorption cross-sections adopted were previously used by Teanby et al. (2013) and derived from the volume absorption coefficients of Anderson and Samuelson (2011). Finally, emission

lines of different gases are present in the far-infrared range and are mainly those of CO, HCN, CH_4, H_2O, C_4H_2 and C_2N_2. The spectral ranges used in the different steps of our retrieval scheme have, however, been selected to only include either CH_4 and its isotopologues (CH_3D and $^{13}CH_4$) or H_2O lines. The vertical profiles of CH_3D and $^{13}CH_4$ we have considered are shown in Figure 2.a and have been calculated using the isotopic ratios determined by Niemann et al. (2010). The choice of the temperature and the H_2O *a priori* profiles will be discussed in the following sections. Note finally that line data were taken from the HITRAN 2004 database (Rothman et al., 2005) and CH_4 line intensities have been revised according to Wishnow et al. (2007). For CIRS, these have been used to calculate k-tables (Lacis and Oinas, 1991) of gaseous opacities (see Teanby et al. (2013) for details) and line-by-line calculations have been performed for the H_2O retrieval. For PACS, given its high spectral resolution, line-by-line calculations have been preferred to the correlated-k method. To decrease the computation time, pre-calculated tables of monochromatic absorption coefficients (hereafter lbl-tables) have been built using the same pressure/temperature grids as for calculating the k-tables.

3.2. Disc-averaged radiance

To analyse both CIRS FP1 (except the nadir spectrum) and PACS observations, it has been necessary to accurately model the disc-averaged radiance. More especially, in the case of CIRS, the inhomogeneous response of the FP1 detector has to be taken into account. It has been shown that the disc-averaged spectrum can be calculated using a weighted sum of spectra simulated for discrete FOV located at increasing offsets from Titan's centre

(Teanby and Irwin, 2007; Teanby et al., 2013). In this work, a total of 20 synthetic spectra distributed from the centre of Titan to the top of the atmosphere has been used to calculate the expected disc-averaged radiance of Titan. The weights applied to the sum are calculated as explained in Teanby et al. (2013). In the case of CIRS observations, these weights are multiplied by the FP1 spatial sensitivity response determined while Cassini was en route to Saturn (Flasar et al., 2004).

4. Analysis strategy

The retrieval of H_2O abundance has been performed using the NEMESIS software (Irwin et al., 2008). This code includes a forward model which can be solved either using a line-by-line model or the correlated-k method (Lacis and Oinas, 1991) according to the spectral resolution of the measurement. A retrieval method is also implemented and is based on the optimal estimation formalism (Rodgers, 2000). The idea of this inverse method is to determine the most probable atmospheric state that is consistent with both the spectrum and the knowledge of the atmosphere prior to the measurement. This is done by minimising a cost function ϕ of the form

$$\phi = \Big(\mathbf{y} - \mathrm{F}(\mathbf{x})\Big)^{\mathrm{T}} \mathbf{S}_{\epsilon}^{-1} \Big(\mathbf{y} - \mathrm{F}(\mathbf{x})\Big) + \Big(\mathbf{x} - \mathbf{x_a}\Big)^{\mathrm{T}} \mathbf{S}_{\mathbf{a}}^{-1} \Big(\mathbf{x} - \mathbf{x_a}\Big), \qquad (1)$$

where $\mathbf{y}$ is the measured spectrum, $\mathbf{x}$ is the atmospheric state vector, $\mathbf{x_a}$ is the *a priori* state vector, $\mathbf{S}_{\epsilon}$ is the measurement covariance matrix (including measurement errors), $\mathbf{S_a}$ is the *a priori* covariance matrix (including the uncertainties on the *a priori* state), and F is the forward model. The

minimisation is performed using an iterative scheme based on the Levenberg-Marquardt method (see Irwin et al. (2008) for more details). Note that in this work, the *a priori* uncertainties are chosen to avoid unconstrained (elements of $\mathbf{S_a}$ are too large) or over-constrained (elements of $\mathbf{S_a}$ are too small) solutions (Irwin et al., 2008).

To analyse CIRS and PACS observations, we have developed a retrieval scheme relying on three successive steps: 1) the retrieval of the tropospheric and stratospheric temperatures, 2) the adjustment of the continuum level in the vicinity of the targeted H_2O lines, and 3) the retrieval of H_2O stratospheric abundance. Because the stratospheric temperatures and the continuum level affect the retrieval of H_2O abundance (see below), their associated uncertainties have been evaluated and then propagated to evaluate the total error on the retrieved H_2O abundance. Each step of the analysis is described in more details in the following sections.

4.1. Step 1: Temperature retrieval

Because it affects the strength of H_2O emission lines along with the H_2O abundance itself, stratospheric temperatures have to be retrieved. As well as affecting the strength of H_2O emission lines, the temperature profile also impacts the vertical sensitivity to H_2O. The lower boundary of this sensitivity is indeed determined by the condensation level of H_2O, whose height depends on the assumed temperature profile. Colder temperatures move this level towards higher altitudes and inversely. For these two reasons, the temperature profile has to be determined before the H_2O retrieval, and more especially in

the pressure range of maximal sensitivity to H_2O. From the H_2O Jacobians[2] shown in Figure 3 (b,d), this range is found to be between 12 and 1 mbar for both disc-averaged CIRS and PACS observations (Jacobians calculated for the CIRS NA spectrum are similar to those of CIRS disc-averaged observations). The temperature over this range of pressure levels is usually retrieved for CIRS observations using the CH_4 ν_4 band of spatially-resolved observations recorded with the FP4 focal planes (e.g. Achterberg et al., 2008, 2011; Vinatier et al., 2010). If these observations are used to build a disc-averaged temperature profile, they have to sample a sufficiently large range of different latitudes and have to be recorded in a same time interval, close to the time of the FP1 disc-averaged observations. This was found to be difficult to achieve. Therefore, we decided to retrieve the whole temperature profile from the far-IR spectrum only. Pure rotational CH_4 lines along with small parts of the continuum level in their vicinity have been used to retrieve stratospheric and tropospheric temperatures. Although this spectral range is mainly sensitive to tropospheric temperatures (Figure 3.a and 3.c), we can see from Figure 3 that the temperature Jacobians calculated for the pure CH_4 rotational lines for both instruments are not null in the 12-1 mbar range, especially close to the level where the Jacobians of H_2O are the largest. CH_4 rotational lines are thus partly sensitive to temperatures in this region and this is what has been exploited in the retrieval. The vertical sensitivity of the temperature retrieval will be discussed in section 5.1. In the case of the CIRS NA spectrum, the temperature is not disc-averaged but has been retrieved using the

[2]Derivatives of the calculated top-of-atmosphere radiance with respect to the H_2O abundances at the 99 levels of the reference atmosphere

same method. In the next subsections, the retrieval settings are described and the method used to assess the errors on the retrieved temperature profile is presented.

4.1.1. Retrieval settings

For CIRS FP1 observations, the continuous temperature profile has been retrieved using six CH_4 lines, which have the largest sensitivity to stratospheric temperature (Figure 5), and including the continuum level in their vicinity (Figure 5). In the case of PACS, fewer lines were available and the temperature has been retrieved from the lines located at 106.43 μm (94 cm^{-1}) and 119.63 μm (83.6 cm^{-1}). In both cases, the retrieval range has been chosen to not include any other lines than CH_4.

Depending on the type of observation, we have considered different *a priori* temperature profiles taking into account the time and the sub-spacecraft latitude at which they were recorded. For CIRS NA and PACS spectra, the *a priori* temperature profile has been set to the temperature profiles respectively assumed by Cottini et al. (2012) and Moreno et al. (2012). Cottini et al. (2012) adopted the temperature profile determined by Anderson and Samuelson (2011) at 15°N. The profile used by Moreno et al. (2012) was a combination of 1) the temperatures measured by the Huygens Atmospheric Structure Instrument (HASI) between 0 km and 140 km (Fulchignoni et al., 2005), 2) the disc-averaged temperatures measured from CIRS (140–500 km) by Vinatier et al. (2010), 3) temperatures retrieved from INMS (1000–1500 km) (De La Haye et al., 2007), and 4) a decreasing temperature from 165 K to 155 K between 500 km and 1000 km. For the disc-averaged CIRS observations, the *a priori* temperature profile has been built using

retrieved profiles from nadir and limb mid-IR CIRS observations (see Figure 6) (Teanby et al., 2016). Briefly, temperature has been retrieved at four pressure levels (5.6, 1 mbar from nadir, 0.1 and 0.01 mbar from limb) and interpolated in time and space to acquire a more global coverage. The temperatures estimated at the sub-spacecraft latitude and at the time of the disc-averaged observations have been interpolated onto a finer pressure grid and have been joined onto the HASI profile (Fulchignoni et al., 2005). The *a priori* uncertainty has been taken at 1% on the whole profile for all the observations.

The measurement covariance matrix $\mathbf{S}_\epsilon$ has been considered diagonal and includes the measurement noise associated with each observations. For CIRS observations, the retrieval has been performed using the correlated-k method. Lbl-tables have been used for PACS spectra. To take into account slight differences between these methods and line-by-line calculations, forward modelling errors have been added to the diagonal elements of the $\mathbf{S}_\epsilon$. They have been estimated from differences between spectra simulated with the different methods using the reference atmosphere described is section 2.

4.1.2. Error analysis

When using the optimal estimation method, the assessment of the retrieval uncertainties is usually performed using the total error covariance matrix, $\mathbf{S} = (\mathbf{K}^{\mathrm{T}}\,\mathbf{S}_\epsilon^{-1}\,\mathbf{K}+\mathbf{S}_\mathbf{a}^{-1})^{-1}$, whose square roots of the diagonal elements correspond to the standard deviation of each retrieved variable included in the retrieved state vector $\mathbf{x_{ret}}$ (i.e., temperature at each pressure level). The use of these errors implies that the elements of the *a priori* covariance matrix are very well known and representative of the real uncertainties on the

a priori profile, which is not the case here. The retrieval random errors have therefore been evaluated using another method. Here, 35 different temperature profiles, covering a large range of temperatures, have been built for each observation. Using these profiles and the reference atmosphere defined in section 3.1, synthetic spectra have been generated and random noise has been added (assuming a normal distribution with a standard deviation equal to the noise associated to the observation). The retrieval procedure described in the previous subsection has then been applied to the 35 spectra and the error has been estimated from the differences between the retrieved and real temperature profiles.

The systematic error related to the choice of the CH_4 profile used in the retrieval has not been estimated from the above analysis. As already mentioned, the CH_4 lines are also sensitive to CH_4 abundance and the latter has been fixed to the profile determined by Niemann et al. (2010). The uncertainties on this profile propagate to the retrieved temperature profile and have to be taken into account. To assess the error propagation, we have shifted the CH_4 profile by $\pm 11\%$ (Niemann et al., 2010) and retrieved the temperature profile again. The systematic errors are taken as the temperature difference between the retrieval with and without applying the shift. It is also worth mentioning that the CH_4 profile determined by Niemann et al. (2010) is measured at one specific location and is not necessarily representative of the observations analysed here. More especially, Lellouch et al. (2014) have observed latitudinal variations of CH_4 stratospheric mole fraction and have estimated that the latter can be as low as 0.01 at some latitudes. For the sake of completeness we have also evaluated the difference in the retrieved

temperature profile if the true stratospheric CH_4 mole fraction is equal to 0.01. These different effects will be discussed in section 5.1. Note finally that there is some error on the intensities of the CH_4 pure rotational lines that we have considered. More especially, there is a 10% reduction of the CH_4 line intensities between Wishnow et al. (2007) and the more recent values reported by Boudon et al. (2010). However, we have evaluated that this difference leads to a maximum uncertainty of 0.06 K on the temperature profile. This uncertainty is insignificant compared with the other sources of error described above, and will be therefore neglected in the calculation of the total uncertainty on the retrieved H_2O abundance.

4.2. Step 2: Continuum

4.2.1. CIRS

The second step of the retrieval scheme consists of properly modelling the continuum level, especially in the vicinity of H_2O lines. Indeed, an under(over)-estimation of this level leads to an over(under)-estimation of the H_2O abundance. This level is mainly affected by tropospheric temperatures, aerosols distribution and absorption, and by the CIA between pairs of N_2, CH_4 and H_2 molecules. The retrieval of the temperature profile described in previous section has partly adjusted this level but we have noticed that differences remain between the simulated and the observed spectra, especially above 120 cm^{-1} where most of the targeted H_2O lines are located. To reduce these differences, we have retrieved a continuous profile of aerosols in a first stage. The *a priori* profile considered is shown in Figure 2.b and the related uncertainties have been set to 20%. The retrieval has been performed using the correlated-k method for the spectral ranges 70-100 cm^{-1} and 130-245

cm^{-1}, avoiding emission lines of gases and noise spikes. As for temperature, forward modelling errors have been included in the $\mathbf{S}_\epsilon$ matrix.

The retrieval of aerosols profile brings a slight improvement to the fit of the continuum level but the latter remains unsatisfactory above 120 cm^{-1}. We have assumed that this was due to uncertainties in the spectral dependence of the absorption cross-sections of haze that we have considered. To properly fit the observed continuum, keeping the retrieved aerosol profile, we have smoothly adjusted the spectral variations of the aerosol absorption cross-sections in the range 120–255 cm^{-1}. Note that apart from variations of haze properties, another possible source for the observed continuum residual is the deficiencies in the modelled CIA (de Kok et al., 2010a), which have not been considered here. However, both aerosols and CIA contribute to the radiance mostly below the emitting level of H_2O and, as long as the continuum level is properly fitted, their values should therefore not impact the H_2O retrieval. Example fits to the CIRS spectra are shown in Figure 5.

4.2.2. PACS/Herschel

Because they are expressed as line/continuum ratios, the analysis performed on CIRS spectra does not need to be applied to PACS H_2O observations. These ratios have however to be converted into disc-averaged radiances. For this, a continuum level has been simulated using the reference atmosphere and using the temperature profile retrieved after the first step. The ratios have then been rescaled using the modelled continuum.

4.3. Step 3: H_2O retrieval

4.3.1. Retrieval settings and a priori choice

The last step of the retrieval scheme consists of determining the stratospheric H_2O abundance. For CIRS observations, this is done using 5 H_2O lines: 132.75, 170.25, 202.75, 208.5, 254 cm^{-1} (identified in Figure 1 and Figure 5), using line-by-line calculations. In the case of PACS, only three lines are used (described in Table 2) and the retrieval is performed using lbl-tables.

According to the optimal estimation method, the *a priori* H_2O profile should represent the best knowledge of the H_2O abundance prior to the measurement. The choice of this profile is important as it will affect directly the H_2O retrieved abundance. This choice is, however, in this case difficult because the uncertainties on the H_2O abundance are large, and their reduction is at the centre of this work. Table 3 and Figure 4 present several profiles that could be used as *a priori*. They are either consistent with previous CIRS observations (Cottini et al., 2012) or with the profile determined from Herschel measurements (Moreno et al., 2012). Because it is impossible to establish which of these is the most representative of the true profile, all of them have been considered as *a priori*. This allows us 1) to assess the effect of the *a priori* profile on the retrieval of H_2O abundance, and 2) to determine if one of them is better suited. Note that we have considered only profiles that differ in values and shape. We have therefore not considered the profiles modelled by Dobrijevic et al. (2014) assuming an external source of CO, which are similar to the "IM1", "IE1" and "IM2" profiles listed in Table 3. The H_2O profiles simulated by Lara et al. (2014) for the comet

impact scenario have not been used because this scenario is very unlikely. To take into account the condensation of H_2O in the low atmosphere, H_2O has been set to its saturation vapor pressure[3] below the condensation level for all the *a priori* profiles. A scaling factor, set at 1 as a first guess, is retrieved for each of them considering 100% of *a priori* uncertainties.

4.3.2. Error analysis - CIRS

The retrieved H_2O abundance is associated to two types of error: 1) the error on the abundance itself, and 2) the uncertainty on the height at which this abundance is located. The first one has been evaluated by propagating the uncertainties of different parameters, and this has been done for the retrieval case using the "IM2" H_2O profile as *a priori*. We have first considered the propagation of the random errors on the retrieved temperature profile and of the measurement noise. For this, the temperature random errors are incorporated in the measurement covariance matrix $\mathbf{S}_\epsilon$ as follows:

$$\mathbf{S}_\epsilon{}' = \mathbf{S}_\epsilon + \mathbf{K}_{\mathrm{Tp}}\,\mathbf{S}_{\mathrm{Tp}}\,\mathbf{K}_{\mathrm{Tp}}^{\mathrm{T}}, \tag{2}$$

where $\mathbf{K}_{\mathrm{Tp}}$ are the temperature Jacobians calculated for the H_2O retrieval range, $\mathbf{S}_{\mathrm{Tp}}$ includes the random errors on temperature estimated according to the method described in subsection 4.1.2. The matrix $\mathbf{S}_\epsilon{}'$ has then been used in the retrieval of H_2O, and the uncertainties on the latter are calculated from the matrix $\mathbf{S}$.

[3]The saturation vapor pressure (P) has been calculated by assuming an expression of the form $P = \exp\left(a+\frac{b}{T}+cT+dT^2\right)$, where T is the temperature and the coefficients a, b, c, d for H_2O are taken equal to 15.278, -5980.3 K, 8.8294×10^{-3} K^{-1} and -1.2169×10^{-5} K^{-2}.

We have then evaluated the error on the retrieved H_2O mole fraction coming from the uncertainty on the continuum level. For this, we have applied a shift to the continuum, representative of the uncertainty of the latter, and retrieved a new H_2O mole fraction. The uncertainty on the continuum has been estimated as the 1σ significance level (68.3%) of the fit described in section 4.2, which is determined by a $\Delta\chi^2$ that depends on the number of retrieved cross-sections (Press et al., 2007).

The last source of errors propagated to the H_2O abundance is the temperature systematic errors coming from the choice of the CH_4 profile. It has been evaluated by shifting the stratospheric temperature by the systematic uncertainties estimated in section 4.1.2 following a change of $\pm 11\%$ of the CH_4 profile. The H_2O retrieval is then performed with the new temperature profile. The difference in the H_2O mole fraction retrieved with and without the shift of temperature is taken as the systematic uncertainty on the H_2O abundance. Note that the H_2O retrieval has also been performed using the stratospheric temperatures retrieved using a CH_4 mole fraction of 0.01. The impact of this change on the determined H_2O abundance will be discussed separately from the systematic errors.

The total uncertainty is finally calculated considering that the random uncertainties (noise, temperature and continuum) are not fully independent of each other, but are independent of the systematic ones resulting from the uncertainty on the CH_4 profile. The random errors have been thus linearly summed and then added to systematic errors by quadrature.

Finally, the height at which H_2O is retrieved is taken as the pressure level at which the Jacobians of H_2O are maximum, which is different for the

different assumed H_2O a priori profile listed in Table 3. The full width at half maximum of these functions has been used to define the uncertainty on that level.

4.3.3. Error analysis - PACS

The assessment of the error on the H_2O abundance retrieved from the PACS observations is very similar to the one applied for CIRS observations, apart from the evaluation of the continuum uncertainty. Because PACS spectra are scaled by a modelled continuum, the continuum level does not need to be fitted and there is no "retrieval" error on this level. However, the modelled continuum is associated with a systematic uncertainty related to the choice of the reference atmosphere, which propagates to the H_2O abundance. To evaluate the propagation of this uncertainty, we have to estimate the error on the modelled continuum, and thus on the parameters affecting this level. For tropospheric temperature, random errors calculated as described in section 4.1.2 are taken into account. For the aerosols distribution and the associated absorption cross-sections, based on the retrieval performed on CIRS spectra, we have estimated that their uncertainties are reasonably around 10% and 20% respectively. A new continuum level has then been modelled by scaling these parameters by their respective uncertainties, and the H_2O abundance has been retrieved from the new radiance spectra computed. The H_2O difference obtained between the two modelled continuum is taken as the systematic uncertainty on H_2O due to the continuum.

5. Results

5.1. Temperature

5.1.1. CIRS disc-averaged

Figure 6 (a-d) shows the *a priori* and retrieved temperature profiles for the four CIRS disc-averaged observations. For all of them, the retrieved profile departs from the *a priori* by about 1.5 K in the troposphere (at pressure levels larger than 100 mbar) and by up to 4 K in the stratosphere (between 100 and 1 mbar) for the 182, 202, 206 observations, and by up to 7 K for the set 219. Figure 5 shows the fit to the set 182 as an example. The vertical sensitivity of the temperature retrieval can be discussed using the associated averaging kernel (AVK) functions (Figure 6 (e-h)). The AVK functions represent the sensitivity of the retrieved state $\mathbf{x_{ret}}$ to the true state $\mathbf{x_{tr}}$ (Rodgers, 2000). The height at which they reach their largest value provides an estimation of the height of the retrieval maximum sensitivity. The AVK are included in a matrix ($\mathbf{A}$) calculated according to:

$$\mathbf{A} = \frac{\partial \mathbf{x_{ret}}}{\partial \mathbf{x_{tr}}} = (\mathbf{K}^{\mathrm{T}}\,\mathbf{S}_{\epsilon}^{-1}\,\mathbf{K} + \mathbf{S}_{\mathbf{a}}^{-1})^{-1}\,\mathbf{K}^{\mathrm{T}}\,\mathbf{S}_{\epsilon}^{-1}\,\mathbf{K}, \tag{3}$$

where $\mathbf{K}$ is the Jacobian matrix of the retrieval. From Figure 6 (e-h), we can see that for the four disc-averaged observations the maximum sensitivity to temperature is found between 400 and 200 mbar as it was expected from the Jacobians (Figure 3.a). The temperature sensitivity stays large up to 70 mbar and then starts to decrease as moving upwards in the atmosphere. In the pressure range of sensitivity to H_2O, the AVK functions still present non zero values and show that the retrieval is also partly sensitive to temperatures

in this region. At pressure levels lower than 1 mbar, where CH_4 lines are not sensitive to temperature (from Jacobians and AVK), the retrieved profile stays close to the *a priori* profile.

The random retrieval error on the temperature profile is shown in Figure 7.a, and has been calculated for the set 182. Given the very similar noise levels and retrieval diagnostics (AVK, DOFS,...), we can reasonably assume that the error will be of the same order of magnitude for the four sets. It decreases from 1 K at the surface to about 0.3 K around 100 mbar, where the maximal sensitivity to temperature is found. It increases then to 0.4 K and stays constant up to 7 mbar, where it starts to increase again to 1 K at 1 mbar. From this level, as the sensitivity of CH_4 lines to temperature decreases, it increases and reaches more than 2 K. The systematic errors on the retrieved temperature profile are shown in Figure 7.b in absolute value for the set 182. We can see that the choice of CH_4 stratospheric abundance has a significant impact on the retrieved temperatures. This is especially the case in the range of sensitivity to H_2O, where the differences reach around 2 K when the CH_4 profile is shifted by $\pm 11\%$ (mole fraction of CH_4 equals 1.32% and 1.64%). In the case where the CH_4 mole fraction is reduced to 0.01, these differences are even larger and reach more than 5 K in the 12-1 mbar range. Note that in this case the retrieved temperature profile is warmer than the *a priori* profile. The impact of the assumed CH_4 profile is of the same order of magnitude for the three other sets. The impact of these temperature differences on the H_2O retrieval will be assessed in subsection 5.2.1.

5.1.2. CIRS nadir

Figure 8.a shows the temperature profile retrieved from the CIRS NA spectrum and the fit is shown in Figure 5. In the troposphere, it is very similar to the *a priori* profile and this was expected since tropospheric temperatures were retrieved by Cottini et al. (2012) using CH_4 pure rotational lines. However, in the 12-1 mbar region, the retrieved profile is significantly different from the profile used by Cottini et al. (2012), which was taken from Anderson and Samuelson (2011) and was not retrieved from the anaylzed spectrum. The differences are up to 8 K. Such temperature difference very likely impacts the retrieval of the stratospheric H_2O abundance and this will be investigated in subsection 5.2.2.

As seen from the AVK functions shown in Figure 8.b, the vertical sensitivity of the retrieval is very similar to the one observed for disc-averaged CIRS spectra. The AVK functions reach their maximum values between 400 and 200 mbar, where the sensitivity to temperature is maximal. Their values then start to decrease, but the retrieval still show sensitivity to temperature in the pressure range of maximum sensitivity to H_2O.

The random uncertainties on the temperature profile are shown in Figure 8.c. They are well below 1 K in the troposphere, especially in the range 400-30 mbar, where the sensitivity to temperature is maximal. In the region of sensitivity to H_2O, these errors are within 0.9-1.6 K, which is slightly larger than the ones estimated for disc-averaged observations. As already noticed in the previous subsection, the CH_4 profile has a large influence on the retrieved profile in the range 12-1 mbar (Figure 8.d). The systematic errors are estimated at around 2 K in absolute value if we consider $\pm 11\%$

of uncertainty on the CH_4 profile. If the stratospheric CH_4 mole fraction is reduced to 0.01, the retrieved temperature profile is warmer by up to 8 K than the one shown in Figure 8.a.

5.1.3. PACS

Figure 9 presents the temperature profile retrieved from PACS observations along with the associated error and vertical sensitivity diagnostics. As observed for the CIRS NA case, the retrieved profile is significantly colder, by up to 9 K, from the temperature profile considered by Moreno et al. (2012) in the range of H_2O sensitivity. As a reminder, Moreno et al. (2012) did not determine the temperature profile from PACS spectra but built one based on several retrievals performed in different studies. The observed difference could possibly lead to the retrieval of a larger H_2O abundance, and then therefore to a better agreement between CIRS and Herschel measurements. This will be discussed in more details in subsection 5.2.3. The fit to the spectrum is shown in Figure 5.

From the AVK functions shown in Figure 9.b, we can see that the retrieval has less vertical resolution than those performed on CIRS observations. The maximum sensitivity to temperature is found to be within 200 and 70 mbar and thus show lower sensitivity to temperature in the lower troposphere. This was expected from the temperature Jacobians (Figure 3.c) and explains that the retrieved profile stays close to the *a priori* in the low atmosphere. As observed for CIRS observations, the retrieval, however, show senstivity to temperature in the pressure range of maximum sensitivity to H_2O. The smaller vertical resolution likely explains the larger random errors on the profile in the 12-1 mbar range, which reach more than 4 K (Figure 9.c).

Systematic errors (absolute value) are within 2-3 K in the same range when the uncertainty on CH_4 profile is assumed to be $\pm 11\%$. If the stratospheric CH_4 mole fraction is reduced to 0.01, the retrieved temperature profile is warmer by up to 9 K. The propagation of these uncertainties to the H_2O abundance will be discussed in section 5.2.3.

5.2. H_2O abundance

Table 4 shows a summary of the H_2O retrievals performed on the different observations analysed in this work. For comparison, the H_2O abundances retrieved when the stratospheric temperatures are determined assuming 1.00% of stratospheric CH_4 are also indicated. Note that they are calculated for the pressure range indicated. Example fits are shown in Figure 5. The following subsections discuss first of all the retrieval for each type of observation and then compare the retrieved H_2O abundances.

5.2.1. CIRS disc-averaged

5.2.1.1 CIRS 182

From Table 4, considering all the different *a priori* H_2O profiles, we can see that the H_2O VMR retrieved from the set 182 is found to be within 0.120 ppb and 0.215 ppb in the 8.2–5.1 mbar pressure range. This shows that the choice of the *a priori* profile has a significant impact on the retrieved H_2O abundance. The total column of H_2O above the condensation level is, however, less affected by the H_2O vertical profile assumptions and is determined to be within 3.5–3.8$\times 10^{14}$ molecules/cm^2. Because the *a priori* profiles have different slopes (Figure 4), they have also an effect on the height of maximum sensitivity to H_2O, which varies from 8.2 mbar to 5.1 mbar. For all

retrievals, the fits are reasonably good with associated χ^2 around 1.48–1.49. Given these very similar values, it is therefore impossible to determine which *a priori* profile is the most appropriate, and all of them are kept in the following discussions. The total error has been estimated at -43%/+44%. The largest contribution to the total error is the uncertainty on the continuum level, which is estimated at ±27%. Finally, when the stratospheric temperatures retrieved using a CH_4 mole fraction of 0.01 are considered, the H_2O VMRs are around 40% smaller and fall within 0.072–0.131 ppb.

5.2.1.2 Other sets

Compared to the set 182, the three other disc-averaged spectra do not show clear H_2O lines as can be seen in Figure 1. Before performing the retrieval, we have first of all assessed if the presence of H_2O lines is statistically attested. To do this, we have calculated the misfit χ^2 as a function of the scaling factor (MF) applied to the H_2O profile (the "IM2" *a priori* profile is considered), starting at MF=0. If H_2O emission lines are present in the spectrum, the χ^2 function should show a minimum at the best fitting scaling factor. Because we are adjusting one parameter (the scaling factor), a 3σ detection requires a χ^2 decrease of 9 compared to the case assuming no H_2O. Figure 10 shows the $\Delta\chi^2\Big(\chi^2 - \chi^2(\mathrm{MF} = 0)\Big)$ functions calculated for each sets. For all of them, the minimum is found below the limit $\Delta\chi^2 = -9$, meaning that H_2O is detected at the 3σ level. The minimum χ^2 is found at MF=0.75 for the set 202, and at MF=0.55 for the sets 206 and 219.

As the presence of H_2O emission lines has been statistically confirmed, we have applied the retrieval scheme to the three sets in a second stage. The

results are summarized in Table 4. The retrieved scaling factors are very close to those determined from the χ^2 analysis: they are equal to 0.76, 0.58 and 0.59 respectively for the sets 202, 206 and 219. These correspond to respective H_2O VMRs of 0.129 ppb, 0.099 ppb, and 0.100 ppb at 5.6 mbar. As seen for the set 182, the choice of the *a priori* H_2O profile has a strong influence, leading to retrieved VMRs varying within 0.080–0.151 ppb for the set 202, 0.059–0.119 ppb for the set 206, and 0.054–0.120 ppb for the set 219, mainly between 8 mbar and 5 mbar. The total columns of H_2O are more stable against the choice of the *a priori* H_2O profile and are found to be within 2.3–2.6$\times10^{14}$ molecules/cm^2, 1.7–2.0$\times10^{14}$ molecules/cm^2, 1.6–2.1$\times10^{14}$ molecules/cm^2 respectively for sets 202, 206, and 219. The assessment of the most appropriate *a priori* is impossible for the three sets because all profiles lead to very similar quality of fit. The reduced χ^2 values are found to be 1.65–1.66, 1.40 and 1.20–1.21 respectively for sets 202, 206 and 219. The estimated total errors are larger than those assessed for the set 182. This was expected given the smaller SNR of the averaged spectra for the three other sets. These errors are equal to -56%/+57%, ±65%, and -70%/+78% respectively for sets 202, 206 and 219. Finally, as seen for set 182, when using the stratospheric temperature profile determined for a stratospheric CH_4 mole fraction of 0.01, the retrieved H_2O VMRs are smaller. They fall within 0.038-0.081 ppb, 0.038-0.082 ppb and 0.032-0.075 ppb respectively for sets 202, 206 and 219.

5.2.2. CIRS nadir

Using the scheme developed for disc-averaged CIRS spectra, the H_2O VMR retrieved from the CIRS NA spectrum falls within 0.058 ppb–0.109 ppb

in the 9.6–5.4 mbar pressure range. This VMR is smaller by a factor 1.3–2.4 than the one determined by Cottini et al. (2012) (0.14 ppb) and this shows the influence of the chosen retrieval scheme on the evaluation of the H_2O abundance. This difference is mostly associated with the choice of the *a priori* profile. Indeed, by redoing the retrieval using a constant H_2O *a priori* profile of 0.1 ppb above the saturation level as Cottini et al. (2012), we retrieve a H_2O VMR of 0.138 ppb, which is in very good agreement with the value reported by Cottini et al. (2012). However, because the H_2O mole fraction has been firmly demonstrated to increase with height, a H_2O profile constant at all altitudes is not the best option for the *a priori* profile and was therefore not considered in this work. Note that if the total errors are taken into account (-42%/+44% for this work, ±0.05 ppb for Cottini et al. (2012)), the largest H_2O abundances determined in this work agree within the error bars with the results of Cottini et al. (2012). Note finally that the discrepancies mentioned above are even larger when the H_2O abundance is retrieved using the stratospheric temperatures determined for a stratospheric CH_4 mole fraction of 0.01. The retrieved H_2O VMRs are in this case a factor of 1.7–3.2 smaller than the one reported by Cottini et al. (2012).

As we already mentioned, the assumed temperature profile affects the height of the H_2O condensation level and therefore the vertical sensitivity to H_2O. Because the temperature profile we retrieved is colder than the one assumed by Cottini et al. (2012), the maximum sensitivity to H_2O is found to be higher in the atmosphere (9.6–5.4 mbar) than determined by Cottini et al. (2012) (maximum sensitivity at 10.7 mbar). Note also that, as seen for CIRS disc-averaged observations, determining the most appropriate H_2O *a*

priori profile is impossible based on the χ^2 values (0.67–0.68 for the reduced χ^2).

5.2.3. PACS

Before applying the retrieval scheme described in section 4 to the PACS observations, we have determined if differences in retrieval codes might have a significant impact on the H_2O abundance. For this, we first retrieved H_2O using very similar retrieval asssumptions as those used by Moreno et al. (2012), i.e., using the same temperature profile and considering the "Sa" profile as *a priori* (Table 3 and Figure 4). With these settings, we retrieve a scaling factor of 0.96 to be applied to the "Sa" profile, which is in excellent agreement with the results of Moreno et al. (2012). To investigate the effect of the choice of the *a priori* profile, we then performed the retrievals using the different profiles shown in Table 3. The retrieved H_2O abundances vary between 0.015–0.031 ppb, and fall well within the error bars estimated by Moreno et al. (2012).

Since differences in retrieval codes do not affect the retrieved H_2O abundance, we have investigated in a second stage if differences in the retrieval method, especially differences in the temperature profile, significantly affect the retrieved H_2O abundance from PACS. For this, we have applied the analysis described in section 4 and the results are shown in Table 4. The retrieved VMRs are found to be within 0.024–0.052 ppb and are slightly larger than those determined by Moreno et al. (2012). This shows the impact of the temperature profile retrieved from PACS CH_4 lines, which was found to be colder than the one assumed by Moreno et al. (2012). This temperature profile also explains that the H_2O maximum sensitivity is found higher in the

atmosphere (8.2–5.6 mbar) because the condensation level moves upwards. The H_2O VMRs retrieved when considering the stratospheric temperature profile determined using 1.00% for the stratospheric CH_4 mole fraction are, however, in good agreement with those determined by Moreno et al. (2012). This is explained by the fact that this temperature profile is very similar to the one considered by Moreno et al. (2012). In this case, the retrieved H_2O VMRs fall within 0.020–0.030 ppb.

As already observed for the other types of observations, the H_2O total column is more stable against the choice of the *a priori* H_2O profile and is determined to be within 0.8–0.9$\times10^{14}$ molecules/cm^2. The total errors are estimated to be -15%/+12%. These errors are significantly smaller than those estimated for CIRS. This can be explained by the better SNR of PACS observations. Note that the reduced χ^2 values are very similar for all the *a priori* profiles and are within 1.49–1.51.

5.2.4. Comparison and discussion

Figure 11 compares the H_2O VMRs retrieved for all observations using the same analysis scheme as a function of the H_2O *a priori* profile considered. We can see that the comparison changes slightly depending on the chosen *a priori*, which directly impacts the retrieved abundance. The lowest VMRs are retrieved using the "Sa" profile of Moreno et al. (2012) (0.029–0.120 ppb), and the largest using the "L3" profile of Lara et al. (2014) (0.052–0.215 ppb). Because it affects the H_2O retrieved abundance, the choice of the *a priori* profile seems to impact the relative agreement between the different observations. Indeed, the best agreement is found for the "Sa" profile, whereas the retrieved VMRs show larger discrepancies in case of "L1", "L2", and

"L3" profiles. Note that in the case of the H_2O total column abundance, there is much less impact of the *a priori* profile on the relative agreement between the different datasets. However, despite the differences due to the choice of the H_2O *a priori* profile and whether the total column abundances or the volume mixing ratios are considered, the same general trend is observed. For each case, the smallest H_2O abundance is retrieved from PACS spectra confirming the initial discrepancy between Moreno et al. (2012) and Cottini et al. (2012). The CIRS disc-averaged set 182 is associated with the largest H_2O abundance, and a very good agreement is found between the three other disc-averaged sets and the CIRS NA observations. Note that the *a priori* profile also impacts the height of maximum sensitivity (Table 4). For each a priori, when taking into account the FWHM of the Jacobians (not shown), PACS and CIRS seem to sound a very similar pressure region, and the small differences do not explain the variation of the retrieved H_2O VMRs between the different observations.

By analysing PACS observations with the same assumptions than Moreno et al. (2012) but with the NEMESIS retrieval code, we have shown that differences in the retrieval codes used by Moreno et al. (2012) and Cottini et al. (2012) hardly explain the differences observed previously between CIRS and PACS measurements. Applying the same retrieval method and making the same H_2O *a priori* assumptions for both PACS and CIRS observations has, on the contrary, decreased the discrepancies observed previously between these instruments (Moreno et al., 2012; Cottini et al., 2012). However, the analysis of the CIRS disc-averaged dataset has brought new differences. Whereas the sets 202, 206, and 219 are in good agreement with the CIRS

NA observation and consistent within the error bars with PACS measurements, the H_2O VMRs retrieved from the set 182 are significantly larger and especially differ from PACS measurements. This is confirmed by Figure 12, which shows a comparison between observed PACS H_2O lines and lines simulated using the H_2O profiles retrieved for the different observations considering the "Sa" *a priori* profile. Indeed, we can see that the profile retrieved for set 182 strongly overestimates PACS H_2O lines. Also from Figure 12 we can see that, although a relative agreement is found within the error bars between the other CIRS and PACS measurements, the H_2O profiles retrieved from CIRS observations are inconsistent with PACS H_2O lines. This confirms that H_2O is less abundant for PACS observations. Based on this, the hypothesis of natural variations of the H_2O abundance, triggered by the global circulation in Titan's atmosphere, can be envisaged. Similarly to nitriles and some hydrocarbons, H_2O shows an increasing mole fraction with height, resulting from a source at high altitudes (either micrometeorite ablation or Enceladus) and a sink in the low atmosphere (condensation and photolysis). The meridional circulation could thus possibly affect the latitudinal distribution of H_2O abundance. This has been observed for nitriles and hydrocarbons, for which subsidence of air rich in these gases leads to an enrichment in the stratosphere, and inversely upwelling leads to the depletion of their stratospheric abundance (e.g. Coustenis et al., 2007, 2016; Teanby et al., 2006, 2008, 2009, 2010). The observations analysed in this work are recorded at different sub-spacecraft latitudes and at different periods in Titan's year (see Figure 11), and are therefore subject to different meridional circulation. The CIRS disc-averaged set 182 is recorded in the

late southern autumn-early southern winter, when according to dynamical models (e.g. Hourdin et al., 2004) the meridional circulation is dominated by a single Hadley cell with subsidence at the South Pole (Teanby et al., 2012) and upwelling at the North Pole. The sub-spacecraft latitude of this set is -41° but because of its disc-averaged nature, the observation includes the South Pole. It is therefore sensitive to the possible H_2O enhancement brought by the subsidence of air rich in H_2O occuring at the South Pole, and this could explain the larger stratospheric VMRs retrieved for this set (see also Coustenis et al. (2016)). On the contrary, PACS observations were recorded close to the northern spring equinox, for which dynamical models predict a transitional circulation state, in which two cells develop with upwelling at the equator and subsidence at both poles (Hourdin et al., 2004; Vinatier et al., 2015). The PACS sub-spacecraft latitude is close to the equator, where upwelling could cause H_2O depletion and explain the low H_2O abundance retrieved from PACS spectra. Note that the variations of H_2O could be very similar to those observed for C_2H_2, which has a comparable lifetime of around 10 years. Another origin that could contribute to explain the H_2O VMRs differences is the spatial/time variation of the input OH/H_2O flux in Titan's atmosphere. Depending on its source, H_2O is likely deposited at different locations (heights but also latitudes) in Titan's atmosphere. The idea of time variations on scales of decades/centuries has already been put forward by Moreno et al. (2012) to explain the difference of the input flux needed to explain current H_2O and CO_2 abundances. Note however that Lara et al. (2014) found this scenario to quantitatively work if the H_2O abundances derived by Cottini et al. (2012) are representative of Titan's water, but not

for the lower abundances reported by Moreno et al. (2012). Time variations of the H_2O source rate at Enceladus, although previously debated, have been reported by some recent studies (Hedman et al., 2013; Nimmo et al., 2014; Teolis et al., 2017, e.g.). These variations occur on timescales of a few months or years, which is smaller than the H_2O lifetime, and unlikely explain the H_2O differences observed in this work. Variations on longer timescales cannot be ruled out, but do not provide a complete satisfactory explanation for the differences observed in this work. Indeed, if such variations existed, variations of the H_2O abundance should be smoothed with a time resolution of around 10 years. The period of time covered by the observations analysed in this work is around 10 years (CIRS NA spectrum recorded in 2004–2008, PACS observations taken in 2010 and the CIRS disc-averaged spectra measured from 2013 to 2015). However, as seen from Figure 13, the H_2O abundance does not vary monotonically with time as it would be expected if the variations were due to time evolution of the OH/H_2O input flux. This is observed for all the *a priori* profiles. For this reason, the meridional circulation and its seasonal variations seem at this stage to provide the most reasonable explanation for the H_2O abundance differences observed in this work. Note also that longitudinal variations of H_2O are barely possible given the lifetime of H_2O and the strong stratospheric zonal winds that rapidly homogenize gas abundances. Finally, following the work of Coustenis et al. (1998), Moreno et al. (2012) reanalysed SWS/ISO observations and determined a H_2O VMR of 0.06 ppb. Most of the H_2O VMRs determined in this work are in good agreement with this reanalysis.

The hypotheses discussed above are hardly proved with the results of this

work, given the very few analysed measurements and the large errors associated with the CIRS observations. The analysis of more observations will be needed in future work to better understand the observed H_2O variations. We also believe that the development of 2D-3D photochemical models, coupling Titan's oxygen chemistry and general circulation, could help address the new issues highlighted in this work. Note that if H_2O is retrieved using stratospheric temperatures determined for a stratospheric CH_4 mole fraction of 0.01, the H_2O VMRs evaluated for the set 182 and for PACS observations remain significantly different, and thus the above discussion still holds. It is worth, however, assessing if this discussion still holds when the CH_4 latitudinal variability is taken into account. Indeed, we have considered a constant stratospheric CH_4 mole fraction for all the observations (either 1.48% or 1.00%). Based on Lellouch et al. (2014), 1.48% seems to be a relatively good assumption for the CIRS disc-averaged set 182. On the contrary, a mole fraction of 1.00% is best suited for the set 219, the CIRS NA observation and for PACS data. If these CH_4 mole fractions are assumed for these observations, the difference in the retrieved H_2O VMRs between set 182 and the three other observations is larger than when considering constant CH_4 abundance, and this strengthens the idea of latitudinal variations of the H_2O abundance. Regarding the sets 202 and 206, it is more difficult to assess what CH_4 mole fraction is the most appropiate, given the large error bars reported by Lellouch et al. (2014). If it is assumed to be in between the extreme values considered in this work, significant differences in the retrieved H_2O VMRs should remain. In future work, attempts to reduce the uncertainty on the stratospheric CH_4 mole fraction, but also on other parameters such as the

continuum level, should be undertaken to reduce the total uncertainty on the retrieved H_2O abundance.

6. Conclusions

The goal of this work was to understand the differences in H_2O abundances retrieved previously by Moreno et al. (2012) from Herschel disc-averaged observations, and by Cottini et al. (2012) from the average of a large number of spectra recorded in a 0–30° latitudinal bin. The strategy for this was to 1) analyse disc-averaged observations of CIRS to investigate if the observation geometry could explain the differences, and 2) (re)analyse the three types of observation with the same retrieval scheme to assess if differences in retrieval codes/methodology could be responsible for the previous discrepancies. For this purpose, four sets of CIRS disc-averaged observations taken between 2013–2015 were analysed. A retrieval scheme composed of three successive steps was also set up. It comprises the retrieval of the temperature profile (step 1), the adjustment of the continuum level in the vicinity of H_2O lines (step 2), and the retrieval of the H_2O abundance (step 3). A rigorous error assessment was performed and included the propagation of the uncertainties of key parameters: measurement noise, temperature, CH_4 profile (for temperature retrieval), and continuum level. Different H_2O *a priori* profiles, either consistent with PACS or CIRS measurements, have been considered for the H_2O retrieval from all observations.

With this analysis, we have first of all shown that differences in the retrieval codes used by Moreno et al. (2012) and Cottini et al. (2012) do not explain the discrepancies observed previously between PACS and CIRS mea-

surements. Applying the same retrieval method, including the temperature retrieval, and making the same H_2O *a priori* assumptions for both PACS and CIRS has, on the contrary, better reconciled the measurements of these instruments, with the agreement depending on the chosen *a priori* H_2O profile. The retrieved H_2O abundances are also in good agreement with the reanalysis of ISO observations performed by Moreno et al. (2012). The addition of the disc-averaged CIRS observations, instead of confirming the consistency between the different datasets, has revealed discrepancies mainly between the set 182 and PACS observations. This makes us question the idea that the datasets should be in agreement. The instruments measured H_2O at different sub-observer latitudes and at different periods in Titan's year which are associated with different meridional circulation. This circulation is shown to affect the latitudinal distribution of nitriles and hydrocarbons, through the subsidence or upwelling of air rich in these gases. As discussed in this work, the meridional circulation could potentially impact the latitudinal distribution of H_2O as well and explain the differences between the CIRS set 182 and PACS measurements. On the contrary, time variations of the OH/H_2O input flux in Titan's atmosphere, which were shown to occur on timescales of a few months or years by recent studies, unlikely explain the observed differences given the H_2O lifetime of around 10 years. Given the few H_2O measurements and the large uncertainties associated with the CIRS observations, these hypotheses are, however, impossible to evaluate with the results obtained so far.

To validate these assumptions, the analysis of more observations will be required in future work. More especially, the NASA Cassini mission covers

now almost the half of a Titan year. CIRS FP1 observations of Titan recorded between 2004 and 2017 could be used to determine if the H_2O abundance varies with time and/or latitude. The photochemical models describing the oxygen chemistry in Titan's atmosphere developed until now are 1D models, considering only the vertical transport of gases. In the future 2D-3D models, coupling the oxygen chemistry with the general circulation, should be developed to address the questions arising from this work. Finally, efforts should be undertaken to decrease the uncertainties on the retrieved H_2O abundances, which are revealed to be large for CIRS observations. Reducing the uncertainty of the stratospheric CH_4 mole fraction or on the continuum level, which were shown to significantly affects the H_2O retrieval, should be a priority of any future study.

Acknowledgements

S. Bauduin would like to thank the Wiener-Anspach Foundation (Belgium) for her postdoctoral fellowship. N. Teanby is funded by UK Science Technology and Facilities Council. C.A. Nixon received funding for his contribution to this work by the NASA Cassini Mission. The authors would like to thank the Cassini and CIRS teams involved in building and testing the instrument, planning data acquisition sequences and calibration of the data. PACS has been developed by a consortium of institutes led by MPE (Germany) and including UVIE (Austria); KU Leuven, CSL, IMEC (Belgium); CEA, LAM (France); MPIA (Germany); INAF-IFSI/OAA/OAP/OAT, LENS, SISSA (Italy); IAC (Spain). This development has been supported by the funding agencies BMVIT (Austria), ESA-PRODEX (Belgium), CEA/CNES (France),

962 DLR (Germany), ASI/INAF (Italy), and CICYT/MCYT (Spain). HCSS /
963 HSpot / HIPE is a joint development (are joint developments) by the Her-
964 schel Science Ground Segment Consortium, consisting of ESA, the NASA
965 Herschel Science Center, and the HIFI, PACS and SPIRE consortia.

966 **References**

967 Achterberg, R. K., Conrath, B. J., Gierasch, P. J., Flasar, F. M., Nixon,
968 C. A., 2008. Titan's middle-atmospheric temperatures and dynamics ob-
969 served by the Cassini Composite Infrared Spectrometer. Icarus 194 (1),
970 263 – 277.

971 Achterberg, R. K., Gierasch, P. J., Conrath, B. J., Flasar, F. M., Nixon,
972 C. A., 2011. Temporal variations of Titans middle-atmospheric tempera-
973 tures from 2004 to 2009 observed by Cassini/CIRS. Icarus 211 (1), 686 –
974 698.

975 Anderson, C. M., Samuelson, R. E., 2011. Titans aerosol and stratospheric
976 ice opacities between 18 and 500m: Vertical and spectral characteristics
977 from Cassini CIRS. Icarus 212 (2), 762 – 778.

978 Borysow, A., 1991. Modeling of collision-induced infrared absorption spectra
979 of H_2-H_2 pairs in the fundamental band at temperatures from 20 to 300
980 K. Icarus 92 (2), 273 – 279.

981 Borysow, A., Frommhold, L., 1986a. Collision-induced rototranslational ab-
982 sorption spectra of N_2-N_2 pairs for temperatures from 50 to 300 K. The
983 Astrophysical Journal 311, 1043–1057.

Borysow, A., Frommhold, L., 1986b. Theoretical collision-induced rototranslational absorption spectra for modeling Titan's atmosphere: H_2-N_2 pairs. The Astrophysical Journal 303, 495–510.

Borysow, A., Frommhold, L., 1986c. Theoretical collision-induced rototranslational absorption spectra for the outer planets: H_2-CH_4 pairs. The Astrophysical Journal 304, 849–865.

Borysow, A., Frommhold, L., 1987. Collision-induced rototranslational absorption spectra of CH_4-CH_4 pairs at temperatures from 50 to 300 K. The Astrophysical Journal 318, 940–943.

Borysow, A., Tang, C., 1993. Far Infrared CIA Spectra of N_2-CH_4 Pairs for Modeling of Titan's Atmosphere. Icarus 105 (1), 175 – 183.

Boudon, V., Pirali, O., Roy, P., Brubach, J.-B., Manceron, L., Auwera, J. V., 2010. The high-resolution far-infrared spectrum of methane at the SOLEIL synchrotron. Journal of Quantitative Spectroscopy and Radiative Transfer 111 (9), 1117 – 1129, special Issue Dedicated to Laurence S. Rothman on the Occasion of his 70th Birthday.

Cottini, V., Nixon, C., Jennings, D., Anderson, C., Gorius, N., Bjoraker, G., Coustenis, A., Teanby, N., Achterberg, R., Bézard, B., de Kok, R., Lellouch, E., Irwin, P., Flasar, F., Bampasidis, G., 2012. Water vapor in Titans stratosphere from Cassini CIRS far-infrared spectra. Icarus 220 (2), 855 – 862.

Coustenis, A., Achterberg, R. K., Conrath, B. J., Jennings, D. E., Marten, A., Gautier, D., Nixon, C. A., Flasar, F. M., Teanby, N. A., Bzard, B.,

1007 Samuelson, R. E., Carlson, R. C., Lellouch, E., Bjoraker, G. L., Romani,
1008 P. N., Taylor, F. W., Irwin, P. G., Fouchet, T., Hubert, A., Orton, G. S.,
1009 Kunde, V. G., Vinatier, S., Mondellini, J., Abbas, M. M., Courtin, R.,
1010 2007. The composition of Titan's stratosphere from Cassini/CIRS mid-
1011 infrared spectra. Icarus 189 (1), 35 – 62.

1012 Coustenis, A., Jennings, D. E., Achterberg, R. K., Bampasidis, G., Lavvas,
1013 P., Nixon, C. A., Teanby, N. A., Anderson, C. M., Cottini, V., Flasar,
1014 F. M., 2016. Titans temporal evolution in stratospheric trace gases near
1015 the poles. Icarus 270, 409 – 420.

1016 Coustenis, A., Salama, A., Lellouch, E., Encrenaz, T., Bjoraker, G., Samuel-
1017 son, R., de Graauw, T., Feuchtgruber, H., Kessler, M., 1998. Evidence
1018 for water vapor in Titan's atmosphere from ISO/SWS data. Astronomy
1019 Astrophysics 336, L85–L89.

1020 Cui, J., Yelle, R., Vuitton, V., Waite, J., Kasprzak, W., Gell, D., Nie-
1021 mann, H., Mller-Wodarg, I., Borggren, N., Fletcher, G., Patrick, E., Raaen,
1022 E., Magee, B., 2009. Analysis of Titan's neutral upper atmosphere from
1023 Cassini Ion Neutral Mass Spectrometer measurements. Icarus 200 (2), 581
1024 – 615.

1025 de Kok, R., Irwin, P., Teanby, N., 2010a. Far-infrared opacity sources in
1026 Titans troposphere reconsidered. Icarus 209 (2), 854 – 857.

1027 de Kok, R., Irwin, P., Teanby, N., Lellouch, E., Bzard, B., Vinatier, S.,
1028 Nixon, C., Fletcher, L., Howett, C., Calcutt, S., Bowles, N., Flasar, F.,

1029 Taylor, F., 2007a. Oxygen compounds in Titan's stratosphere as observed
1030 by Cassini CIRS. Icarus 186 (2), 354 – 363.

1031 de Kok, R., Irwin, P., Teanby, N., Nixon, C., Jennings, D., Fletcher, L.,
1032 Howett, C., Calcutt, S., Bowles, N., Flasar, F., Taylor, F., 2007b. Char-
1033 acteristics of Titan's stratospheric aerosols and condensate clouds from
1034 Cassini CIRS far-infrared spectra. Icarus 191 (1), 223 – 235.

1035 de Kok, R., Irwin, P., Teanby, N., Vinatier, S., Tosi, F., Negrao, A., Osprey,
1036 S., Adriani, A., Moriconi, M., Coradini, A., 2010b. A tropical haze band
1037 in Titans stratosphere. Icarus 207 (1), 485 – 490.

1038 De La Haye, V., Waite, J. H., Johnson, R. E., Yelle, R. V., Cravens, T. E.,
1039 Luhmann, J. G., Kasprzak, W. T., Gell, D. A., Magee, B., Leblanc,
1040 F., Michael, M., Jurac, S., Robertson, I. P., 2007. Cassini Ion and Neu-
1041 tral Mass Spectrometer data in Titan's upper atmosphere and exosphere:
1042 Observation of a suprathermal corona. Journal of Geophysical Research:
1043 Space Physics 112 (A7), A07309.

1044 Dobrijevic, M., Hébrard, E., Loison, J., Hickson, K., 2014. Coupling of oxy-
1045 gen, nitrogen, and hydrocarbon species in the photochemistry of Titan's
1046 atmosphere. Icarus 228, 324 – 346.

1047 English, M., Lara, L., Lorenz, R., Ratcliff, P., Rodrigo, R., 1996. Ablation
1048 and chemistry of meteoric materials in the atmosphere of Titan. Advances
1049 in Space Research 17 (12), 157 – 160.

1050 Flasar, F. M., Kunde, V. G., Abbas, M. M., Achterberg, R. K., Ade, P.,
1051 Barucci, A., Bézard, B., Bjoraker, G. L., Brasunas, J. C., Calcutt, S.,

et al., 2004. Exploring the Saturn System in the Thermal Infrared: The Composite Infrared Spectrometer. Space Science Review 115, 169–297.

Fulchignoni, M., Ferri, F., Angrilli, F., Ball, A., et al., 2005. In situ measurements of the physical characteristics of Titan's environment. Nature 438 (7069), 785–91.

Hansen, C., Esposito, L., Stewart, A., Meinke, B., Wallis, B., Colwell, J., Hendrix, A., Larsen, K., Pryor, W., Tian, F., 2008. Water vapour jets inside the plume of gas leaving enceladus. Nature 456 (27), 477–479.

Hansen, C. J., Esposito, L., Stewart, A. I. F., Colwell, J., Hendrix, A., Pryor, W., Shemansky, D., West, R., 2006. Enceladus' Water Vapor Plume. Science 311 (5766), 1422–1425.

Hansen, C. J., Shemansky, D. E., Esposito, L. W., Stewart, A. I. F., Lewis, B. R., Colwell, J. E., Hendrix, A. R., West, R. A., Waite, J. H., Teolis, B., Magee, B. A., 2011. The composition and structure of the Enceladus plume. Geophysical Research Letters 38 (11), L11202.

Hartogh, P., Lellouch, E., Moreno, R., Bockelée-Morvan, D., Biver, N., Cassidy, T., Rengel, M., Jarchow, C., Cavali, T., Crovisier, J., Helmich, F., Kidger, M., 2011. Direct detection of the Enceladus water torus with Herschel. A&A 532, L2.

Hedman, M. M., Gosmeyer, C. M., Nicholson, P. D., Sotin, C., Brown, R. H., Clark, R. N., Baines, K. H., Buratti, B. J., Showalter, M. R., 2013. An observed correlation between plume activity and tidal stresses on Enceladus. Nature 500 (7461), 182–184.

1075 Hörst, S. M., Vuitton, V., Yelle, R. V., 2008. Origin of oxygen species in
1076 Titan's atmosphere. Journal of Geophysical Research: Planets 113 (E10),
1077 E10006.

1078 Hourdin, F., Lebonnois, S., Luz, D., Rannou, P., 2004. Titan's stratospheric
1079 composition driven by condensation and dynamics. Journal of Geophysical
1080 Research: Planets 109 (E12), E12005.

1081 Irwin, P., Teanby, N., de Kok, R., Fletcher, L., Howett, C., Tsang, C., Wil-
1082 son, C., Calcutt, S., Nixon, C., Parrish, P., 2008. The NEMESIS planetary
1083 atmosphere radiative transfer and retrieval tool. Journal of Quantitative
1084 Spectroscopy and Radiative Transfer 109 (6), 1136 – 1150.

1085 Jennings, D. E., Flasar, F. M., Kunde, V. G., Nixon, C. A., Segura, M. E.,
1086 Romani, P. N., Gorius, N., Albright, S., Brasunas, J. C., Carlson, R. C.,
1087 Mamoutkine, A. A., Guandique, E., Kaelberer, M. S., Aslam, S., Achter-
1088 berg, R. K., Bjoraker, G. L., Anderson, C. M., Cottini, V., Pearl, J. C.,
1089 Smith, M. D., Hesman, B. E., Barney, R. D., Calcutt, S., Vellacott, T. J.,
1090 Spilker, L. J., Edgington, S. G., Brooks, S. M., Ade, P., Schinder, P. J.,
1091 Coustenis, A., Courtin, R., Michel, G., Fettig, R., Pilorz, S., Ferrari, C.,
1092 Jun 2017. Composite infrared spectrometer (cirs) on Cassini. Appl. Opt.
1093 56 (18), 5274–5294.

1094 Lacis, A. A., Oinas, V., 1991. A description of the correlated k distribution
1095 method for modeling nongray gaseous absorption, thermal emission, and
1096 multiple scattering in vertically inhomogeneous atmospheres. Journal of
1097 Geophysical Research: Atmospheres 96 (D5), 9027–9063.

Lara, L., Lellouch, E., González, M., Moreno, R., Rengel, M., 2014. A time-dependent photochemical model for Titan's atmosphere and the origin of H_2O. A&A 566, A143.

Lellouch, E., Bézard, B., Flasar, F., Vinatier, S., Achterberg, R., Nixon, C., Bjoraker, G., Gorius, N., 2014. The distribution of methane in Titan's stratosphere from Cassini/CIRS observations. Icarus 231, 323 – 337.

Moreno, R., Lellouch, E., Lara, L. M., Feuchtgruber, H., Rengel, M., Hartogh, P., Courtin, R., 2012. The abundance, vertical distribution and origin of H_2O in Titan's atmosphere: Herschel observations and photochemical modelling. Icarus 221 (2), 753 – 767.

Niemann, H. B., Atreya, S. K., Demick, J. E., Gautier, D., Haberman, J. A., Harpold, D. N., Kasprzak, W. T., Lunine, J. I., Owen, T. C., Raulin, F., 2010. Composition of Titan's lower atmosphere and simple surface volatiles as measured by the Cassini-Huygens probe gas chromatograph mass spectrometer experiment. Journal of Geophysical Research: Planets 115 (E12).

Nimmo, F., Porco, C., Mitchell, C., 2014. Tidally Modulated Eruptions on Enceladus: Cassini ISS Observations and Models. The Astronomical Journal 148 (3), 46.

Poglitsch, A., Waelkens, C., Geis, N., Feuchtgruber, H., Vandenbussche, B., Rodriguez, L., Krause, O., Renotte, E., van Hoof, C., Saraceno, P., et al., 2010. The Photodetector Array Camera and Spectrometer (PACS) on the-Herschel Space Observatory. A&A 518, L2.

Press, W. H., Teukolsky, S. A., Vetterling, W. T., Flannery, B. P., 2007. Numerical Recipes: The Art of Scientific Computing, 3rd Edition. Cambridge University Press.

Rodgers, C., 2000. Inverse methods for atmospheric sounding: theory and practice. World Scientific.

Rothman, L., Jacquemart, D., Barbe, A., Benner, D. C., Birk, M., Brown, L., Carleer, M., Chackerian, C., Chance, K., Coudert, L., Dana, V., Devi, V., Flaud, J.-M., Gamache, R., Goldman, A., Hartmann, J.-M., Jucks, K., Maki, A., Mandin, J.-Y., Massie, S., Orphal, J., Perrin, A., Rinsland, C., Smith, M., Tennyson, J., Tolchenov, R., Toth, R., Auwera, J. V., Varanasi, P., Wagner, G., 2005. The HITRAN 2004 molecular spectroscopic database. Journal of Quantitative Spectroscopy and Radiative Transfer 96 (2), 139 – 204.

Samuelson, R. E., Maguire, W. C., Hanel, R. A., Kunde, V. G., Jennings, D. E., Yung, Y. L., Aikin, A. C., 1983. CO_2 on Titan. Journal of Geophysical Research: Space Physics 88 (A11), 8709–8715.

Teanby, N., Irwin, P., de Kok, R., Nixon, C., 2009. Dynamical implications of seasonal and spatial variations in Titan's stratospheric composition. Philosophical Transactions of the Royal Society of London A: Mathematical, Physical and Engineering Sciences 367 (1889), 697–711.

Teanby, N., Irwin, P., de Kok, R., Nixon, C., Coustenis, A., Bézard, B., Calcutt, S., Bowles, N., Flasar, F., Fletcher, L., Howett, C., Taylor, F., 2006.

1143 Latitudinal variations of HCN, HC_3N, and C_2N_2 in Titan's stratosphere
1144 derived from Cassini CIRS data. Icarus 181 (1), 243 – 255.

1145 Teanby, N., Irwin, P., de Kok, R., Nixon, C., Coustenis, A., Royer, E., Cal-
1146 cutt, S., Bowles, N., Fletcher, L., Howett, C., Taylor, F., 2008. Global and
1147 temporal variations in hydrocarbons and nitriles in Titan's stratosphere
1148 for northern winter observed by Cassini/CIRS. Icarus 193 (2), 595 – 611.

1149 Teanby, N., Irwin, P., Nixon, C., Courtin, R., Swinyard, B., Moreno, R.,
1150 Lellouch, E., Rengel, M., Hartogh, P., 2013. Constraints on Titan's mid-
1151 dle atmosphere ammonia abundance from Herschel/SPIRE sub-millimetre
1152 spectra. Planetary and Space Science 75, 136 – 147.

1153 Teanby, N., Irwin, P., Nixon, C., de Kok, R., Vinatier, S., Coustenis, A.,
1154 Sefton-Nash, E., Calcutt, S., Flasar, F., 2012. Active upper-atmosphere
1155 chemistry and dynamics from polar circulation reversal on Titan. Nature
1156 491, 732–735.

1157 Teanby, N. A., Irwin, P., 2007. Quantifying the effect of finite field-of-view
1158 size on radiative transfer calculations of Titan's limb spectra measured by
1159 Cassini-CIRS. Astrophysics and Space Science 310 (3-4), 293–305.

1160 Teanby, N. A., Irwin, P. G. J., de Kok, R., Nixon, C. A., 2010. Seasonal
1161 Changes in Titan's Polar Trace Gas Abundance Observed by Cassini. The
1162 Astrophysical Journal Letters 724 (1), L84.

1163 Teanby, N. A., Vinatier, S., Sylvestre, M., de Kok, R., Nixon, C., Irwin,
1164 P., 2016. Titan's south polar stratospheric vortex evolution. In: DPS48,
1165 509.08.

1166 Teolis, B. D., Perry, M. E., Hansen, C. J., Waite, J. H., Porco, C. C., Spencer,
1167 J. R., Howett, C. J. A., 2017. Enceladus Plume Structure and Time Vari-
1168 ability: Comparison of Cassini Observations. Astrobiology 17 (9), 926–940.

1169 Tomasko, M., Doose, L., Engel, S., Dafoe, L., West, R., Lemmon, M.,
1170 Karkoschka, E., See, C., 2008. A model of Titan's aerosols based on
1171 measurements made inside the atmosphere. Planetary and Space Science
1172 56 (5), 669 – 707.

1173 Vinatier, S., Bézard, B., Lebonnois, S., Teanby, N. A., Achterberg, R. K.,
1174 Gorius, N., Mamoutkine, A., Guandique, E., Jolly, A., Jennings, D. E.,
1175 Flasar, F. M., 2015. Seasonal variations in Titan's middle atmosphere dur-
1176 ing the northern spring derived from Cassini/CIRS observations. Icarus
1177 250, 95 – 115.

1178 Vinatier, S., Bézard, B., Nixon, C. A., Mamoutkine, A., Carlson, R. C.,
1179 Jennings, D. E., Guandique, E. A., Teanby, N. A., Bjoraker, G. L., Flasar,
1180 F. M., Kunde, V. G., 2010. Analysis of Cassini/CIRS limb spectra of Titan
1181 acquired during the nominal mission. Icarus 205 (2), 559 – 570.

1182 Waite, J. H., Combi, M. R., Ip, W.-H., Cravens, T. E., McNutt, R. L.,
1183 Kasprzak, W., Yelle, R., Luhmann, J., Niemann, H., Gell, D., Magee,
1184 B., Fletcher, G., Lunine, J., Tseng, W.-L., 2006. Cassini Ion and Neutral
1185 Mass Spectrometer: Enceladus Plume Composition and Structure. Science
1186 311 (5766), 1419–1422.

1187 Wishnow, E., Orton, G., Ozier, I., Gush, H., 2007. The distortion dipole

rotational spectrum of CH_4: A low temperature far-infrared study. Journal of Quantitative Spectroscopy and Radiative Transfer 103 (1), 102 – 117.

Table 1: Sets of CIRS FP1 disc-averaged observations analysed in this work. The start and end times are in UTC and Titan radius is the projected angular radius of the solid surface. The sub-spacecraft latitudes and Titan radius are the average of each sequence. TEA stands for Titan Explorations at Apoapse.

TEA	**Start date**	**End date**	**No. spectra**	**Sub-spacecraft latitude**	**Titan radius (mrad)**
182-001	21/02/2013 8:31:38	22/02/2013 04:21:23	712	-41.43°	1.64
202-001	02/03/2014 22:47:21	03/03/2014 11:56:10	898	50.73°	1.69
206-001	10/07/2014 00:50:30	10/07/2014 12:29:06	793	48.58°	1.67
219-001	23/07/2015 13:57:21	24/07/2015 01:35:55	792	-0.02°	1.63

Table 2: PACS observations of CH_4 and H_2O (see also Moreno et al. (2012)) analysed in this work.

Gas	**Line (μm)**	**Spectral resolution (μm)**	**Start date**	**Duration (sec)**	**Sub-observer lat/lon**
H_2O	66.43	0.0169	22/06/2010 23:49:52	3071	2.10°/283.74°
	75.38	0.039	22/06/2010 22:56:26	3079	2.10°/282.91°
	108.07	0.1127	22/06/2010 22:56:26	3079	2.10°/282.91°
CH_4	106.43	0.1120	23/06/2010 00:43:14	1140	2.10°/284.59°
	119.63	0.1176	23/06/2010 00:43:14	1140	2.10°/284.59°

Table 3: *A priori* profiles considered for the H_2O retrieval (see also Figure 4).

Reference	Name	Type	Agreement	Comments
Moreno et al. (2012)	Sa	Measured	Herschel	Parametrized profile: $q = q_0 \times (p_0/p)^n$ with n the power law index
Dobrijevic et al. (2014)	IM1	Modelled	Herschel	Origin H_2O: micrometeorite ablation OH flux: 5.7×10^5 cm^{-2} s^{-1}
Dobrijevic et al. (2014)	IM2	Modelled	CIRS	Origin H_2O: micrometeorite ablation OH flux: 2.6×10^6 cm^{-2} s^{-1}
Dobrijevic et al. (2014)	IE1	Modelled	Herschel	Origin H_2O: Enceladus OH flux: 1.4×10^6 cm^{-2} s^{-1}
Lara et al. (2014)	L1	Modelled	Herschel	Time-dependent model, initial OH flux: 5.1×10^6 cm^{-2} s^{-1} + loss to the haze
Lara et al. (2014)	L2	Modelled	CIRS	Time-dependent model, initial OH flux: 5.1×10^6 cm^{-2} s^{-1} + loss to the haze
Lara et al. (2014)	L3	Modelled	CIRS	Time-dependent model, initial OH flux: 1.0 or 2.0×10^7 cm^{-2} s^{-1}

Table 4: Retrieved H_2O abundances and associated errors for the different observations analysed. The retrieved abundances are indicated for the two temperature profiles considered in this work. The given ranges describe the results arising from using the different *a priori* H_2O profiles listed in Table 3. Note that the pressure range is defined using the pressure levels at which the H_2O sensitivity is maximum (based on H_2O Jacobians). The total column of H_2O is calculated above the condensation level. For the comparison, the reported H_2O VMRs for the case using 1.00% of stratospheric CH_4 are given for the same pressure range.

Observation	H_2O VMR (ppb)	Total error	Pressure (mbar)	H_2O total column (molec/cm^2)	H_2O VMR (ppb) if 1.00% CH_4	Previous retrieved H_2O
CIRS 182	0.120–0.215	-43%/+44%	8.2–5.1	3.5–3.8×10^{14}	0.072–0.131	/
CIRS 202	0.080–0.151	-56%/+57%	8.2–5.1	2.3–2.6×10^{14}	0.038–0.081	/
CIRS 206	0.059–0.119	-65%/+65%	8.0–5.1	1.7–2.0×10^{14}	0.038–0.082	/
CIRS 219	0.054–0.120	-70%/+78%	8.2–4.7	1.6–2.1×10^{14}	0.032–0.075	/
CIRS NA	0.058–0.109	-42%/+44%	9.6–5.4	2.0–2.2×10^{14}	0.044–0.082	0.14±0.05 ppb at 10.7 mbar
PACS	0.024–0.052	-15%/+12%	8.2–5.6	0.8–0.9×10^{14}	0.020–0.030	0.023±0.006 ppb at 12.1 mbar

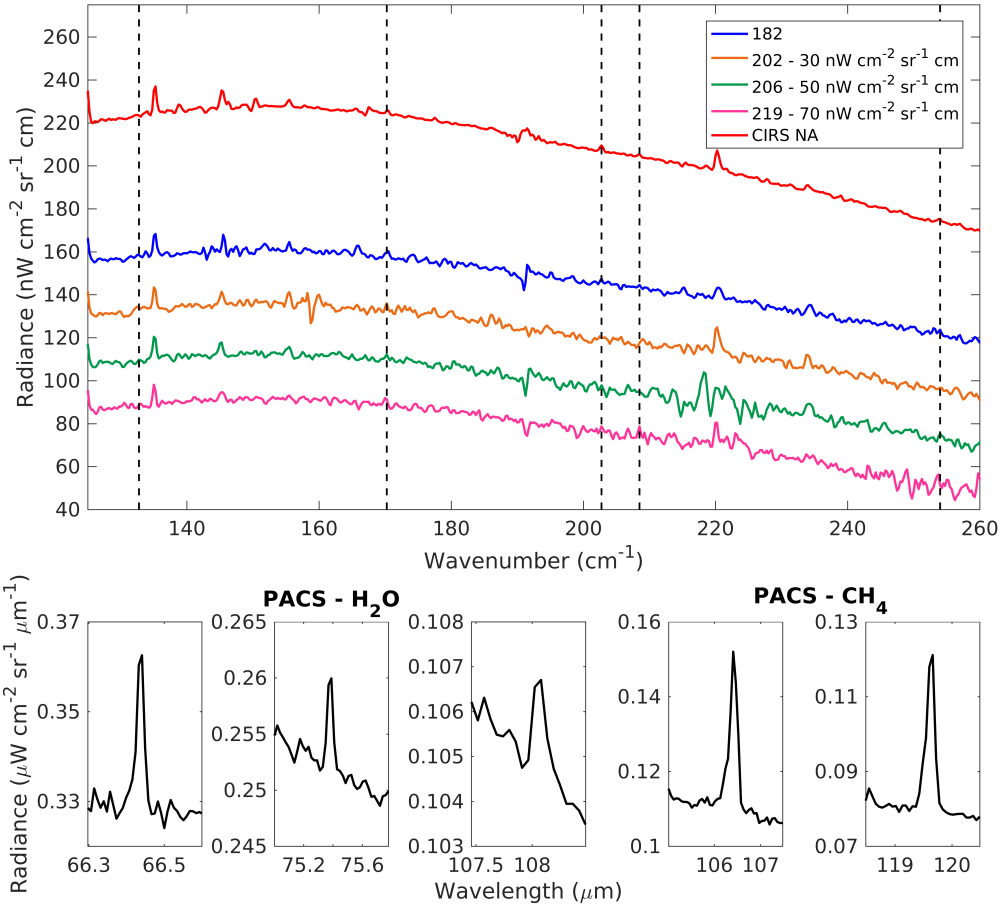

Figure 1: CIRS and PACS spectra analysed in this work. For display purposes, CIRS disc-averaged spectra have been offset vertically as indicated. H_2O lines, which are used for the retrieval, are identified for CIRS spectra with vertical dashed lines. PACS spectra are expressed in radiance units (μW cm^{-2} sr^{-1} μm^{-1}) as explained in the text.

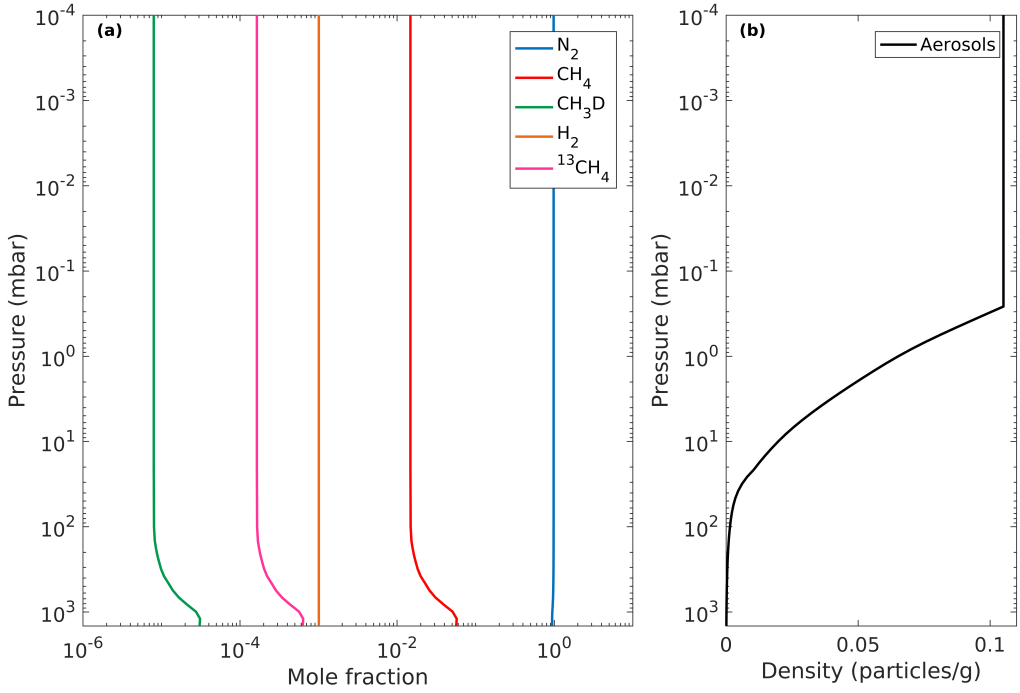

Figure 2: Main reference atmospheric vertical profiles used to simulate CIRS and PACS spectra: (a) Mole fraction of gases (Niemann et al., 2010), (b) Haze specific density (de Kok et al., 2007b, 2010b; Tomasko et al., 2008). See text for details.

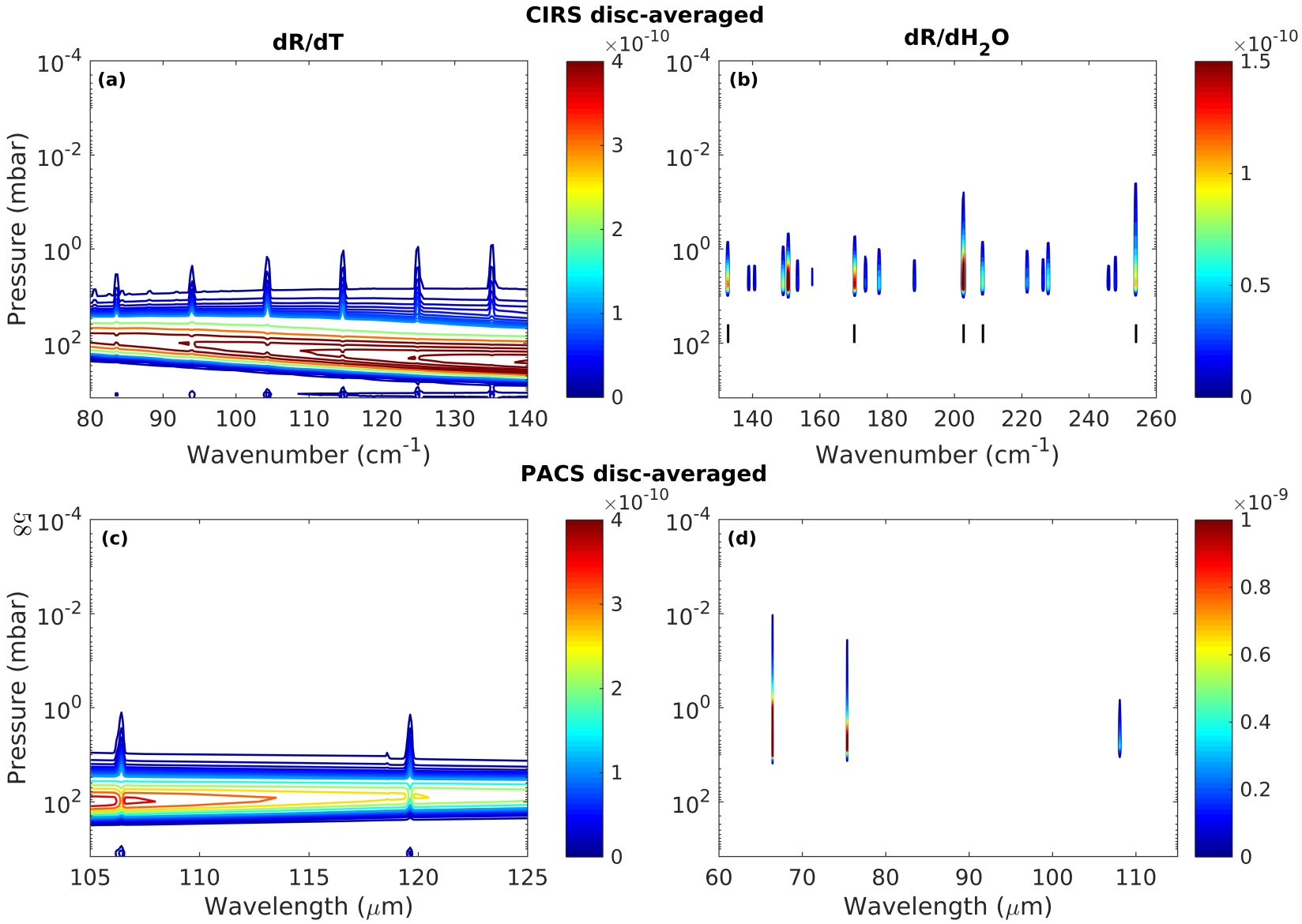

Figure 3: Jacobians of temperature and H_2O (color scales) calculated for disc-averaged observations of CIRS (a,b) and PACS (c,d). The Jacobians of H_2O are calculated for the "IM2" *a priori* profile (see Table 3 and Figure 4). For CIRS, the H_2O lines used in the retrieval are indicated with the vertical black lines.

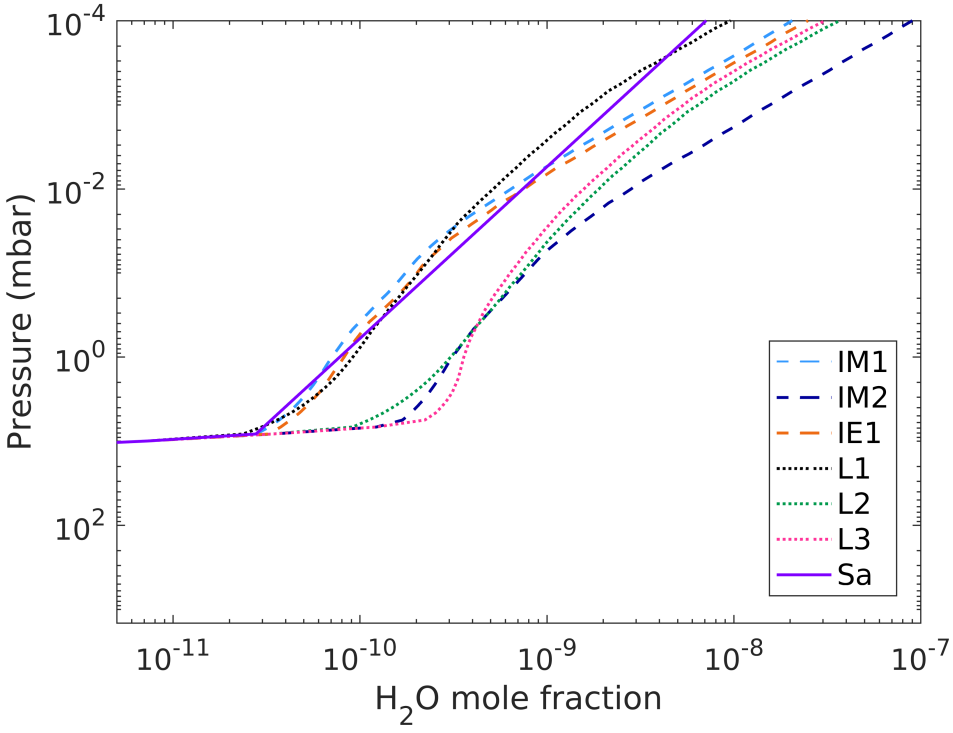

Figure 4: *A priori* profiles of H_2O considered in this work (see Table 3 for details).

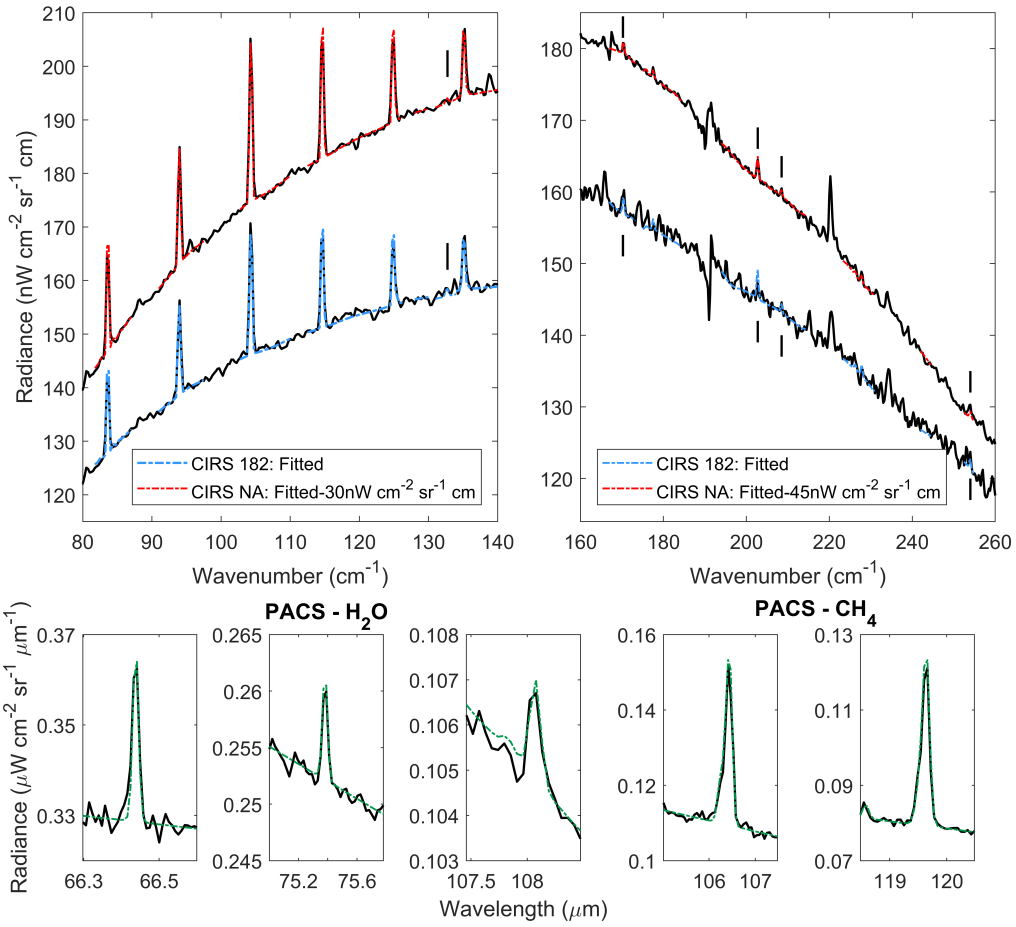

Figure 5: Example fits to the observed CIRS (set 182 and CIRS NA) and PACS spectra. For CIRS observations, they include the fits of the temperature retrieval, of the continuum and of the H_2O retrieval (considering the "IM2" *a priori* profile). Vertical lines indicate the fitted H_2O lines. For display purposes, the CIRS NA spectrum has been offset vertically as indicated. For PACS, the fits are shown for the H_2O and CH_4 lines analysed (considering the "Sa" *a priori* profile).

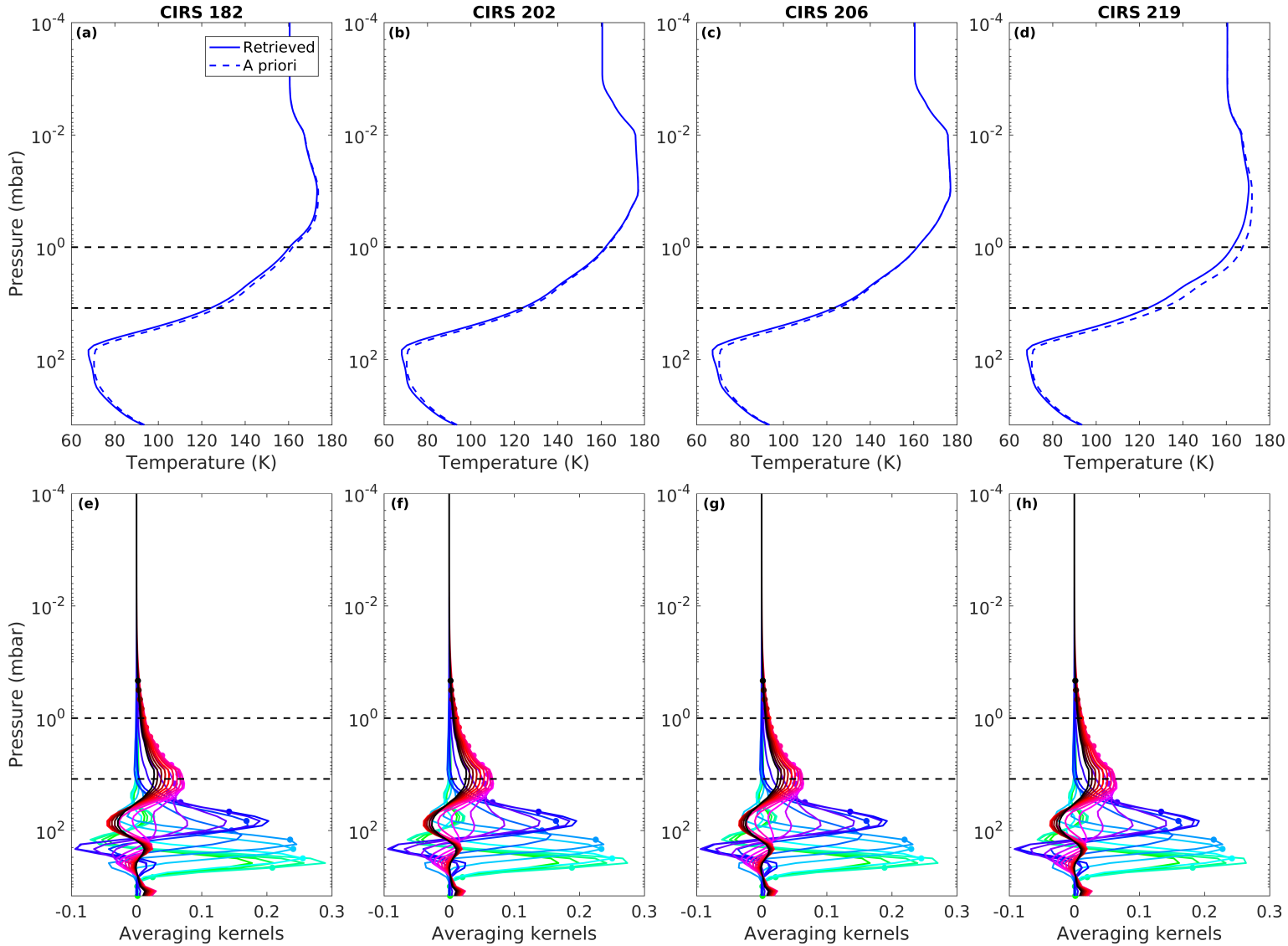

Figure 6: Retrieved and *a priori* temperature profiles (a-d) and associated averaging kernels functions (e-h) for the four sets of disc-averaged CIRS spectra. The black dashed lines delimit the region of maximum sensitivity to H_2O (12-1 mbar). For clarity, only one in every two averaging kernel functions until 0.2 mbar are shown. The dots indicate the pressure levels associated to each of these functions and a different colour is associated to each AVK function.

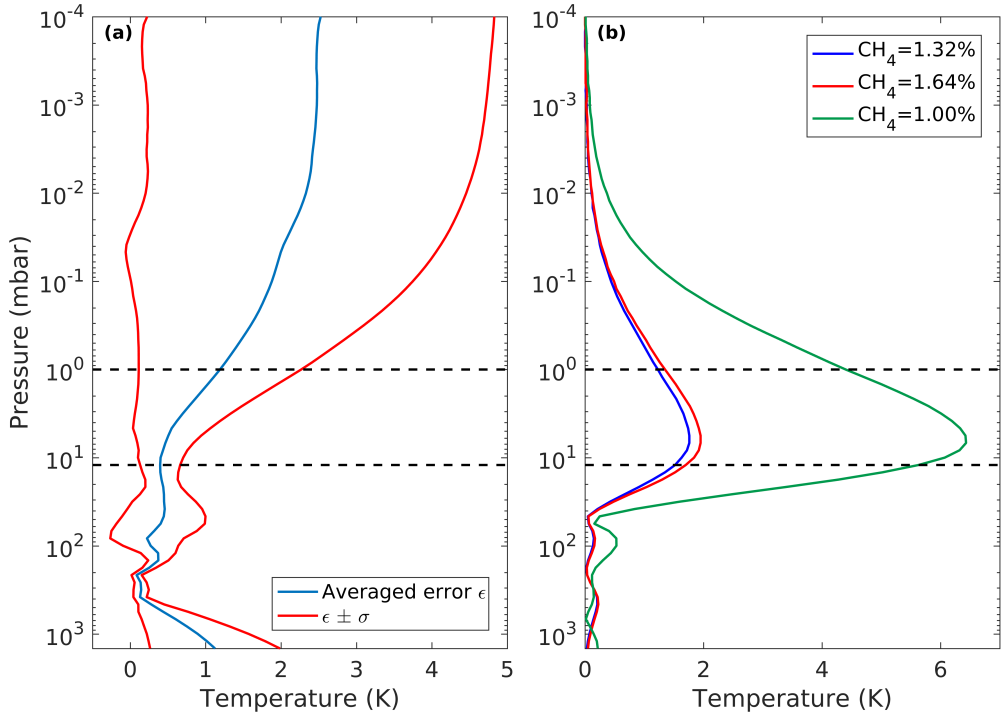

Figure 7: (a) Random error and its standard deviation calculated from retrievals on synthetic spectra. (b) Systematic errors (absolute values) on the retrieved temperature profile associated with the choice of CH_4 profile. The black dashed lines delimit the stratospheric region of sensitivity to H_2O abundance.

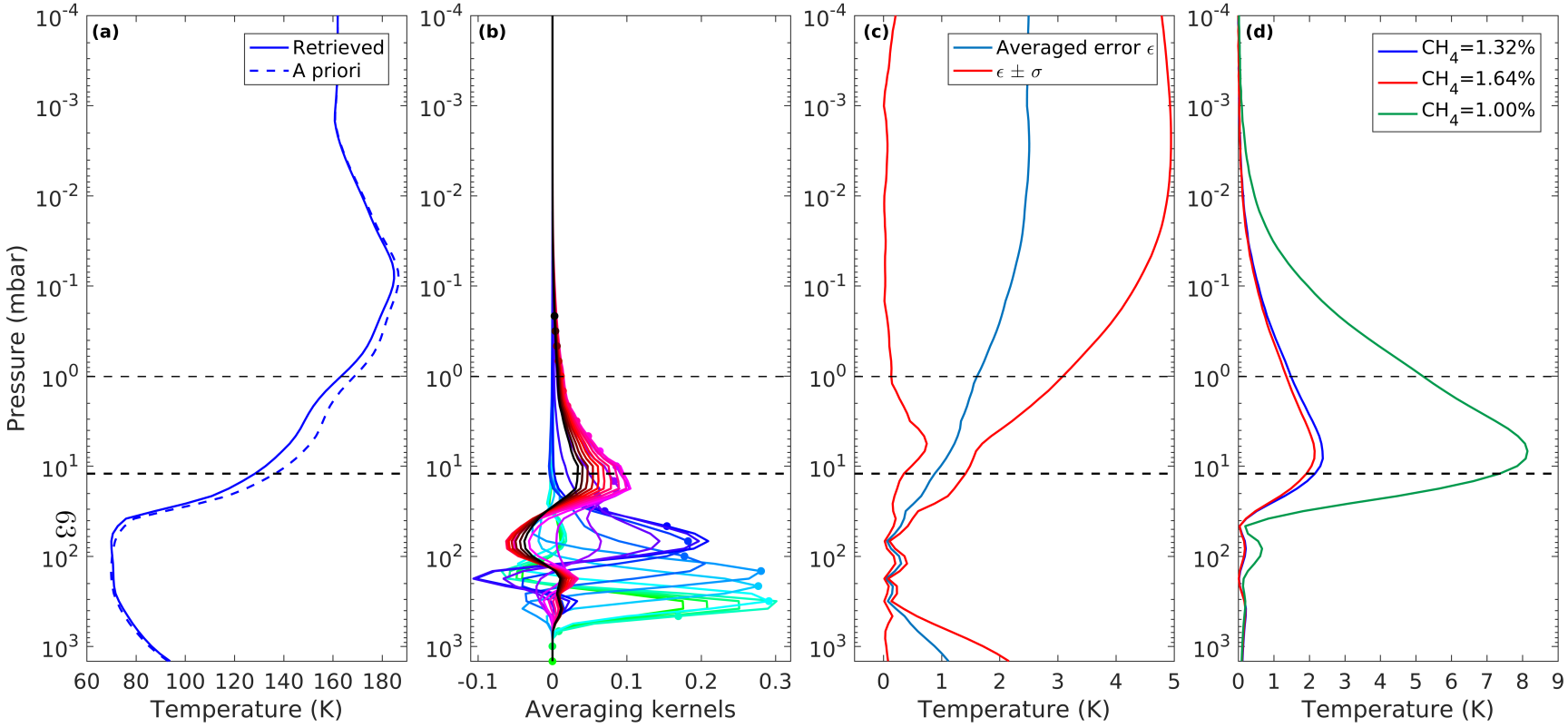

Figure 8: Temperature retrieval from the CIRS NA spectrum: (a) *A priori* and retrieved profile, (b) AVK functions associated to the retrieved profile, (c) Random errors and its standard deviation calculated from retrievals on synthtic spectra, and (d) Systematic errors (absolute values) on the retrieved temperature profile associated to the choice of CH_4 profile. The black dashed lines delimit the stratospheric region of sensitivity to H_2O abundance.

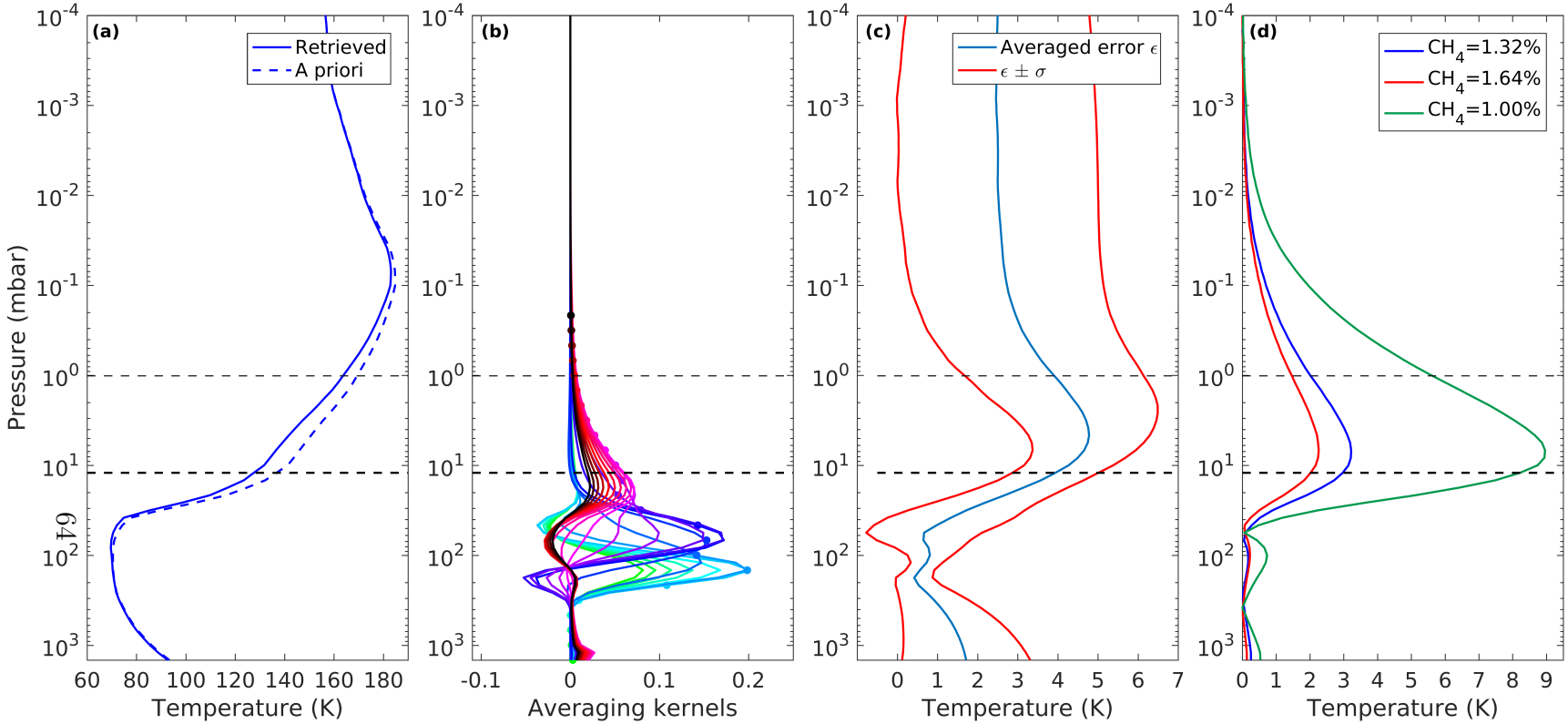

Figure 9: Same as Figure 8 but for PACS observations.

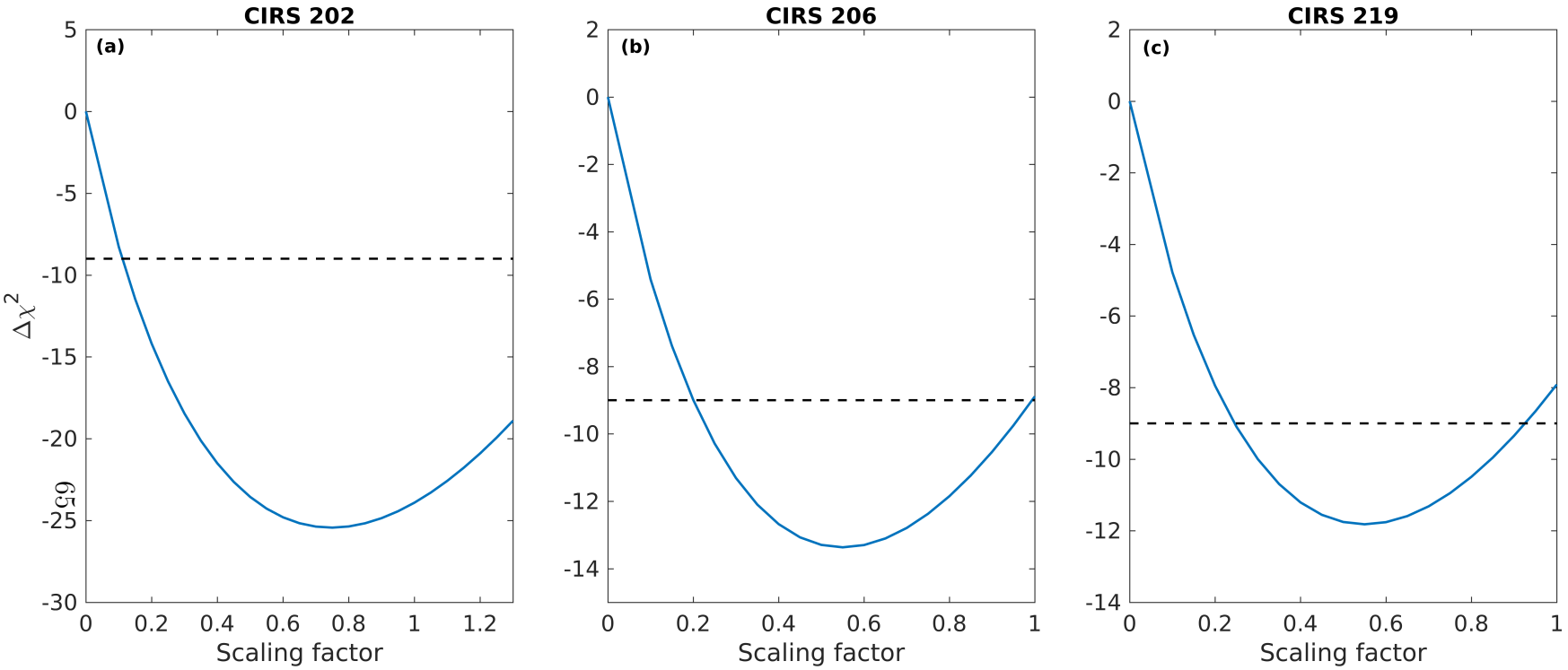

Figure 10: $\Delta\chi^2\Big(\chi^2 - \chi^2(\mathrm{MF}=0)\Big)$ as a function of the scaling factor applied to the "IM2" H_2O *a priori* profile for the CIRS sets 202 (a), 206 (b), and 219 (c). The horizontal dashed line indicates the level of 3σ detection ($\Delta\chi^2 = -9$).

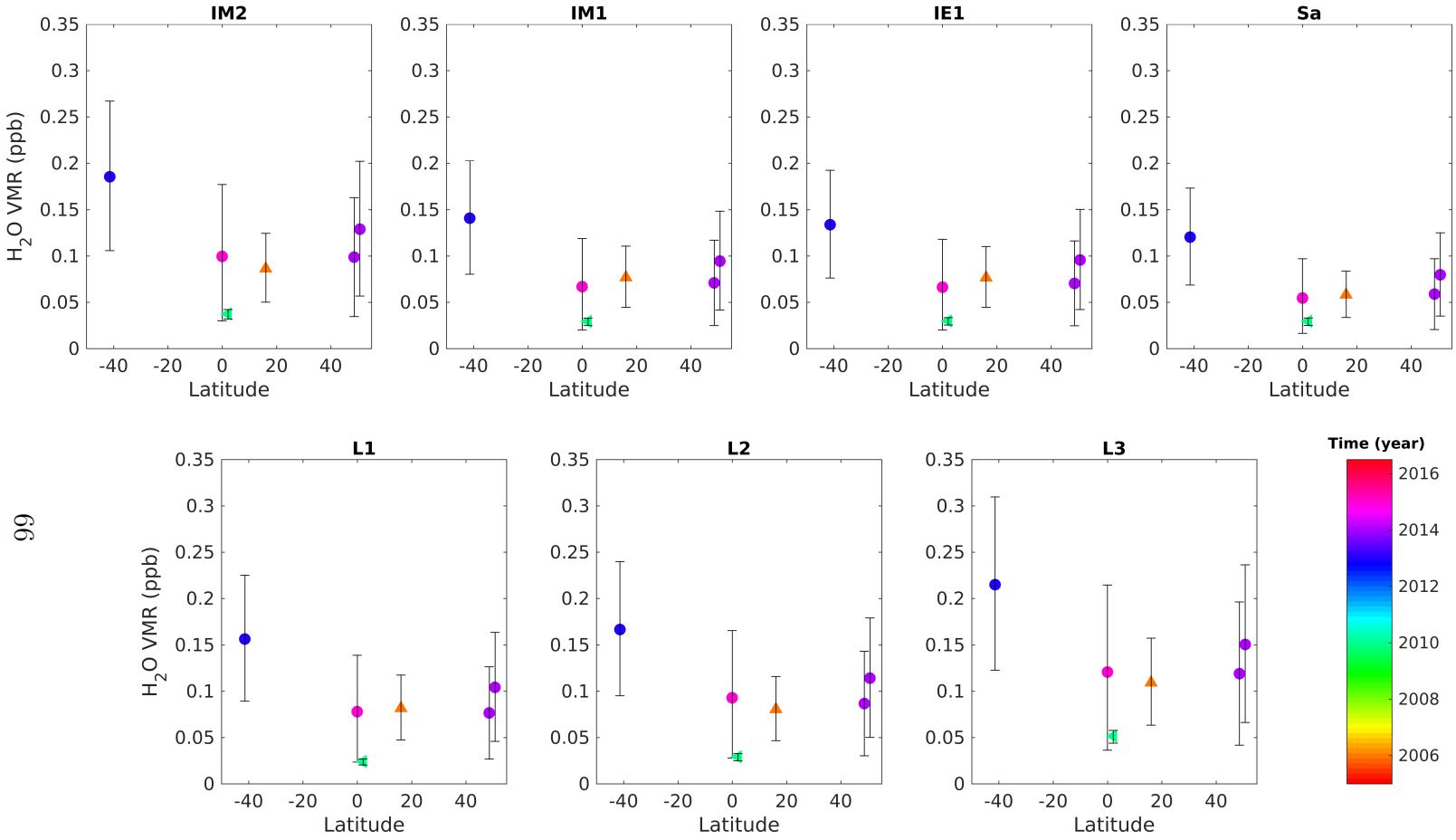

Figure 11: Retrieved H_2O VMRs for all observations as a function of latitude, of time (color scale) and of the *a priori* H_2O profile. These VMRs are retrieved using the stratospheric temperature profile determined using 1.48% for the stratospheric CH_4 mole fraction. The circles represent CIRS disc-averaged observations, the upward-pointing triangle the CIRS nadir observation, and the left-pointing triangle PACS observations.

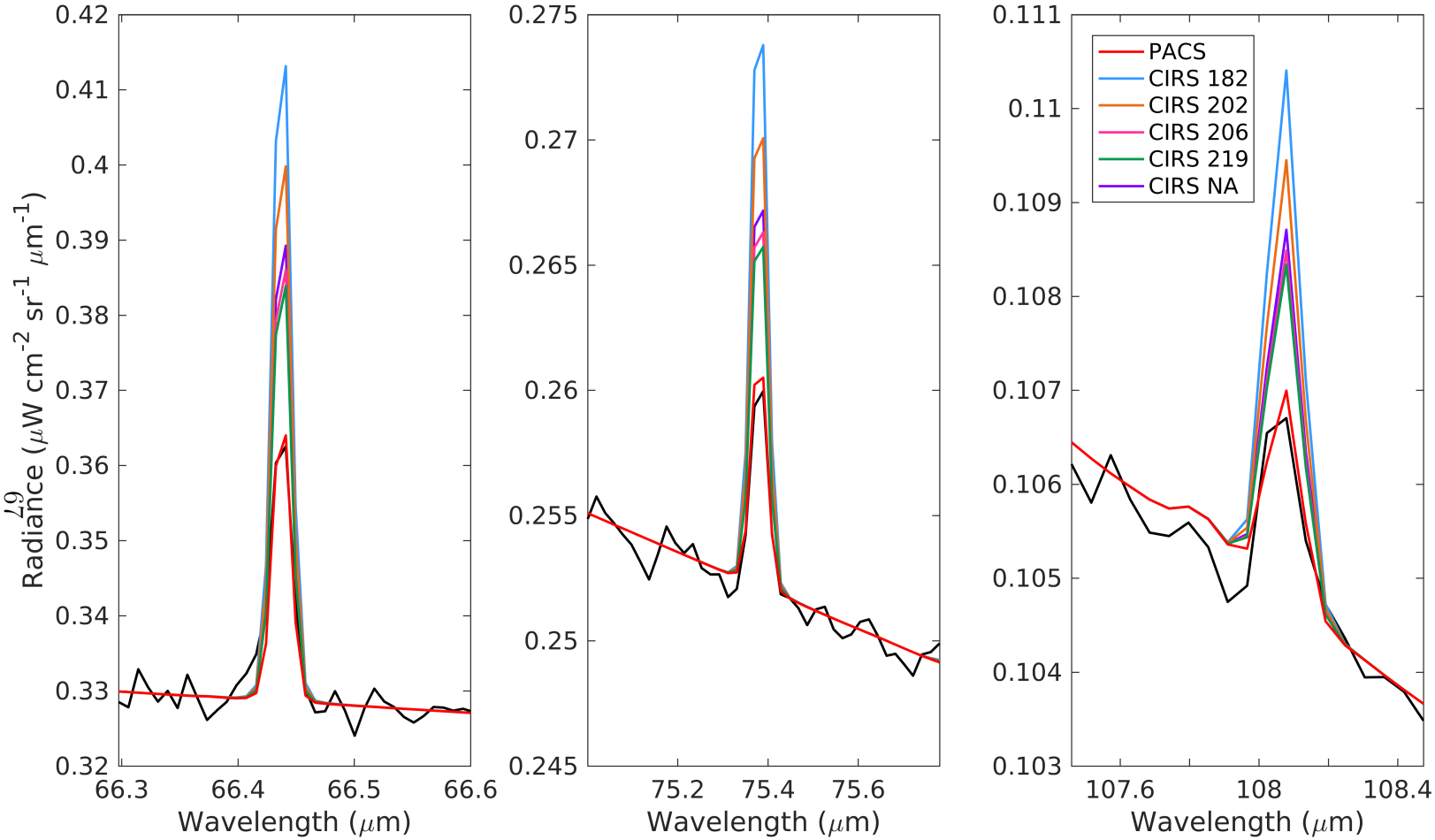

Figure 12: Comparison between observed PACS H_2O lines (black) and lines simulated using the H_2O profiles retrieved for the different observations (colored lines). The case using the "Sa" *a priori* profile has been considered (the profile has been scaled by the retrieved scaling factors) and using the stratospheric temperature profile determined using a stratospheric CH_4 mole fraction of 1.48%.

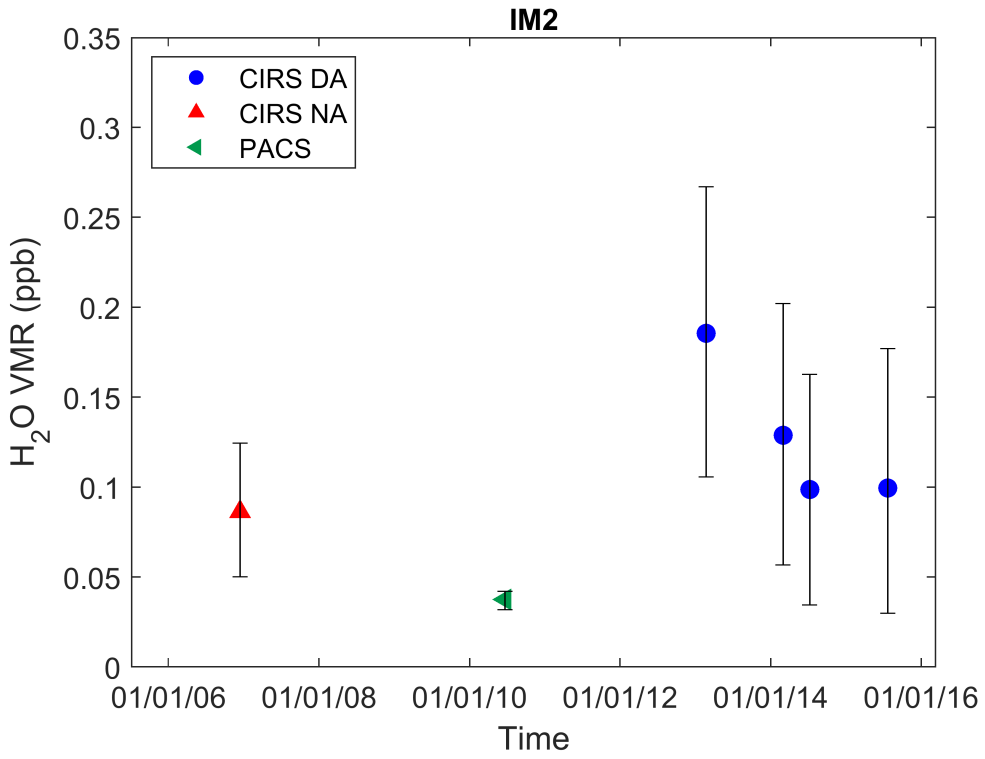

Figure 13: Time variations of the retrieved H_2O abundances for the case using the "IM2" *a priori* profile and using the stratospheric temperature profile determined using 1.48% for the stratospheric CH_4 mole fraction.